DOI 10.1007/s11148-023-00746-9
Refractories and Industrial Ceramics *Vol. 63, No. 4, November, 2022*

STRENGTHENING AND REINFORCING OF CERAMIC-METALLIC MATERIALS BY QUATERNARY SOLID SOLUTIONS OF METALLIC PHASES DURING SPARK PLASMA SINTERING

A. V. Hmelov[1,2]

Translated from *Novye Ogneupory*, No. 8, August, 2022, pp. 35 – 52.

Original article submitted July 28, 2022.

The article shows the effect of mixtures of metal powders of Ti, Nb, Cr, Zr and Ti, Mo, Cr, V, as well as Mo, Nb, Cr, and Ta during spark plasma sintering of compositions at a pressing load of 85 MPa in the range of 1200 – 1600°C on the phase composition, microstructure, grains sizes of crystalline phases, relative density, linear shrinkage, physico-mechanical properties, linear correlation, values of standard deviations of the modulus of elasticity and fracture toughness of mullite–(Ti,Ta)(C,N)–B_4C–*c*-BN samples. Synthesized powders of TiC, TiN, B_4C, and *h*-BN are characterized by different intensity of crystallization of TiC, TiN, B_4C, and *h*-BN phases, respectively. Spark-plasma sintered solid solution of (Ti,Ta)(C,N) shows intensive crystallization of the (Ti,Ta)(C,N) phase at 1500°C, as well as crystalline, uniform, and densely sintered microstructure. Sintered samples with the mixtures of metal powders show similar mullitization and crystallization of the (Ti,Ta)(C,N), B_4C, and *c*-BN phases with different evolution of the crystalline β-Ti, Nb, Cr, Zr, β-Ti, Mo, Cr, V, and β-Mo, Nb, Cr, Ta phases in the range of 1200 – 1600°C. The microstructures of sintered samples are crystalline, variously uniform and variously densely sintered. The samples with mixtures of metal powders form variously dispersed granular compositions of crystalline phases in the range of 1200 – 1600°C, different uniformity, density, path, width of boundary layers of solid solutions of metallic phases, different packing of particles of non-oxide and solid solutions of metallic phases, have different path and width of propagating microcracks at the boundaries of ceramic particles and particles of solid solutions of metallic phases at 1300 and 1500°C, as well as across the boundary layers of solid solutions of metallic phases at 1500°C. This differently affects the ingrowth and values of physico-mechanical properties, crack resistance linear correlation, values of standard deviations of the modulus of elasticity and fracture toughness in the range of 1200 – 1600°C.

Keywords: mullite–(Ti,Ta)(C,N)–B_4C–*c*-BN, mixtures of Ti, Nb, Cr, Zr, Ti, Mo, Cr, V and Mo, Nb, Cr, and Ta powders, spark plasma sintering.

INTRODUCTION

The development and implementation in practical application of ceramic-metal (cermet) mate-rials are associated with a number of problems, such as the difference of diffusion processes, mechanisms, homogeneity, completeness and intensity of crystallization of solid solutions of ceramic and metallic phases, as well as homogeneity and completeness of sintering of ceramic and metallic powders or their mixtures, and especially the areas of particles of heterogeneous solid solutions and boundary layers [1 – 5]. As a result, separately crystallize solid solutions of ceramic and metallic phases of different densities due to the lack of incorporation of metallic powders into ceramic components, formed in different scale sintered and uniform microstructures, boundary layers of different density, uniformity, path, width in the conditions of low pressing load and sintering temperature, which generally determines the embrittlement or strengthening, reinforcing the structures of boundary layers of ceramic and metallic areas [2 – 5]. These microstructural features affect the brittle-to-elastic property ratio; initiation, activation, or deceleration of microcracks propagation, the variety, path rectilinear, tortuous, continuous, discontinuous), length and width of

[1] Riga Technical University, Institute of Silicate Materials, Riga, Latvia.
[2] aleksejs.hmelov44@gmail.com

microcrack; absence or presence of a "bridge" in the boundary layers of ceramic and metallic regions, which inhibits the propagation of microcracks; decrease or increase of the values of properties of materials [3 – 5].

Strengthening and reinforcing of the boundary structure of grains of cermet materials by adding separate metal powders (e.g., Ti, V, W and Mo) to ceramic compositions is caused by the formation of different density of non-oxide compounds during reactions between non-oxide components and metallic powder, in this case the strengthening and reinforcing effect varies greatly depending the density of the structures of the resulting non-oxide components [2 – 5].

An effective method of strengthening and reinforcing of the boundary structure of grains of cermet material is associated with the addition to ceramic compositions the mixtures of the metal powders: Zr and Mo, Zr and Ta [6]. Strengthening and reinforcing by such additives are caused by the formation of particles of solid solutions of metallic phases (e.g., α-, β-Mo, Zr; α-, β-Zr, Ta / α-, β-Ta, Zr) during the incorporation the structures of metallic components in the solid state [6]. Crystallization of brittle intermetallic compounds, such as Mo_2Zr, Ta_3Zr/Ta_3Zr_2, forming agglomerates of various density and sizes, reduces rigidity and hardness at the boundaries of ceramic and metallic grains, initiate the propagation of microcracks in the boundary layers of ceramic and metallic phases [6].

A more modern and promising method of strengthening and reinforcing of the boundary structure of grains of the cermet material is based on the combination of mixtures of metal powders of W and Mo, Zr and Ti with additives of β-Si_3N_4, *c*-BN and solid solution TiC–ZrC [7]; Ni and Ta, Ni and Zr with additives of TiC and *c*-ZrO_2, and solid solution TaB_2–NbC [8]; and powders of metal compounds, such as Ti_2AlNb, NiTi, NiNbZr and NiVTa with additives of *c*-ZrO_2, *c*-BN and solid solution (Ti, Mo)(C,N) [9]. The combination of non-oxide/oxide – non-oxide additives with solid solutions, obtained from the corresponding intermediate materials during spark plasma sintering, contributes the incorporation of hard particles of non-oxide/oxide – non-oxide additives and solid solutions into the intergranular space of ceramic and metallic grains, which increase compaction, rigidity, and hardness and inhibition the propagation of microcracks in the boundary areas of these grains [7 – 9]. The strengthening and reinforcing of the boundary structure of the grains by these additives significantly depends on the per-centage content of β-Si_3N_4, *c*-BN, β-SiAlON, *c*-ZrO_2, *c*-BN, and current component in the solid solutions, and the ratio of these additives [7 – 9]. The differences in the used metal powder mixtures and intermetallic compounds are associated with the types and mechanisms of reactions, in particular solid-phase reactions in the presence of W and Mo, Zr and Ti [7], NiNbZr, NiVTa [9], as well as liquid-phase reactions with the presence of Ni and Ta, Ni and Zr [8], Ti_2AlNb and NiTi [9]. During solid-phase sintering of the compositions with W and Mo, Zr and Ti, NiNbZr, and NiVTa, intermetallic compounds and solid solutions of the metal phases are formed by direct interaction and incorporation of metallic components [7, 9], while during liquid-phase sintering of the compositions with Ni and Ta, Ni and Zr; Ti_2AlNb, NiTi — via low-melting eutectics in the systems Ni–Ta, Ni–Zr, Ti_3Al–Nb, and Ni–Ti, which differently effect on the solid-/liquid-phase sintering of ceramic and metal powders, density, uniformity, width, path, crack resistance of the boundary layers, as well as physico-mechanical properties of materials [7 – 9].

The objective of this work is to study the effect of mixtures of metal powders of Ti, Nb, Cr; Zr, Ti, Mo, Cr, V; Mo, Nb, Cr, and Ta during spark plasma sintering of the compositions at a pressing load of 85 MPa in the range of 1200 – 1600°C on the phase composition, microstructure, grain sizes of crystalline phases, relative density, linear shrinkage, physico-mechanical properties, linear correlation, values of standard deviations of the modulus of elasticity, and fracture toughness of mullite–(Ti,Ta)(C,N)–B_4C–*c*-BN samples.

EXPERIMENTAL

To prepare a mixture of Al_2O_3 and SiO_2 powders, Al_2O_3 (Aldrich, Belgium, 97.5% purity) and SiO_2 (Merck, Germany, 97.5% purity) were used. These components were measured according to a weight ratio corresponding to mullite stoichiometry (3:2) and mixed in a planetary mill (RETSCH PM 400) for about 10 min.

The synthesis of TiC, TiN, TaB_2, B_4C, and *h*-BN powders was performed in a plasma-chemical apparatus under vacuum at 1600°C for 1 hour using the initial components (Table 1).

The synthesis of TiC, TiN, TaB_2, B_4C, and *h*-BN powders was performed according to the following reactions:

$$TiO_2 + 2C \rightarrow TiC + CO_2, \quad (1)$$

$$TiO_2 + N_2 \rightarrow TiN + NO_2, \quad (2)$$

$$2B_2O_3 + 4C \rightarrow B_4C + 3CO_2, \quad (3)$$

$$2B_2O_3 + 3.5N_2 \rightarrow 4h\text{-}BN + 3NO_2, \quad (4)$$

$$3TaO_2 + 10B \rightarrow 3TaB_2 + 2B_2O_3. \quad (5)$$

The weight ratios of the initial components used to prepare TiC, TiN, B_4C, *h*-BN, and TaB_2 powders and metal powder mixtures are shown in Table 2. The content of the initial components in the mixtures of metal powders was calculated based on the quaternary equilibrium phase diagrams of Ti–Nb–Cr–Zr, Ti–Mo–Cr–V, and Mo–Nb–Cr–Ta [10 – 12].

Sintered (Ti,Ta)(C,N) was prepared by the spark plasma sintering method (SPS, Summimoto, model SPS 825. CE, Dr. Sinter, Japan) from TiC and TiN melts with TaB_2 additive

TABLE 1. Characteristics of initial components.

Obtained powder	Initial components	Manufacturer	Purity, %
TiC	TiO_2/C	Merck, Germany / Aldrich, Belgium	98.5/99.0
TiN	TiO_2/N_2	Merck, Germany / Aldrich, Belgium	98.5/99.5
TaB_2	TaO_2/B	Aldrich, Belgium / Aldrich, Belgium	99.0/98.5
B_4C	B_2O_3/C	Merck, Germany / Aldrich, Belgium	99.0/98.0
h-BN	B_2O_3/N_2	Aldrich, Belgium / Aldrich, Belgium	99.0/99.5
Ti	Ti	Merck, Germany	99.0
Nb	Nb	Aldrich, Belgium	98.5
Cr	Cr	Merck, Germany	99.0
Zr	Zr	Aldrich, Belgium	99.5
Mo	Mo	Merck, Germany	99.0
V	V	Aldrich, Belgium	99.5
Ta	Ta	Merck, Germany	99.5

TABLE 2. Initial component ratios.

Powders/powder mixtures	Initial components	Initial component weight ratios, g per 100 g of mixture
TiC	TiO_2/C	76.90/23.10
TiN	TiO_2/N_2	74.03/25.97
B_4C	B_2O_3/C	73.89/26.11
h-BN	B_2O_3/N_2	57.99/42.01
TaB_2	TaO_2/B	86.47/13.53
Ti, Nb, Cr, Zr	Ti, Nb, Cr, Zr	14.21/27.42/29.98/28.39
Ti, Mo, Cr, V	Ti, Mo, Cr, V	13.96/27.92/30.15/27.97
Mo, Nb, Cr, Ta	Mo, Nb, Cr, Ta	64.75/10.45/14.62/10.18

under vacuum (60 kPa), pressing load of 30 MPa, soaking time of 10 min, temperature range of 2130 – 2280°C, and heating rate of 230°C/min. The initial component ratio (composition $(Ti_{0.6}Ta_{0.4})(C_{0.7}N_{0.3})$) was calculated based on the ternary equilibrium phase diagram of TiC–TiN–TiB_2 in the region of molten components of hyper-eutectic (close to eutectic) composition [13]: mass of components (35 mol.% TiC/15 mol.% TiN/50 mol.% TaB_2) = 16,00 / 7,11 / 76,89 g per 100 g of the mixture; TiC / TiN / TaB_2 ratio = 2,25 / 1 / 10,8.

Sintered (Ti,Ta)(C,N) was crushed in a planetary mill (RETSCH PM 400) for 30 min to obtain a powder with a particle size ranging from 5 to 10 μm.

Powders of B_4C, *h*-BN, sintered (Ti,Ta)(C,N) and metal powder mixtures were mixed at the corresponding weight ratios (Table 3) in a planetary mill (RETSCH PM 400) for about 10 min.

The weight ratios of ceramic components and metal powder mixtures per 100 g of the mixture were as follows: $M40(Ti_{0.6}Ta_{0.4})(C_{0.7}N_{0.3})5B_4C5BN10Ti10Nb19,5Cr10,5Zr$ — 3,89, $M40(Ti_{0.6}Ta_{0.4})(C_{0.7}N_{0.3})5B_4C5BN8,5Ti8,5Mo17Cr16V$ — 4,32, $M40(Ti_{0.6}Ta_{0.4})(C_{0.7}N_{0.3})5B_4C5BN30Mo5Nb12,5Cr2,5Ta$ — 3,21.

The resulting mixture of Al_2O_3 and SiO_2 powders was mixed with the prepared groups of powder mixtures $(Ti_{0.6}Ta_{0.4})(C_{0.7}N_{0.3})/B_4C/h$-BN/Ti/Nb/Cr/Zr, $(Ti_{0.6}Ta_{0.4})(C_{0.7}N_{0.3})/B_4C/h$-BN/Ti/ Mo/Cr/V, and $(Ti_{0.6}Ta_{0.4})(C_{0.7}N_{0.3})/B_4C/h$-BN/Mo/Nb/Cr/Ta in a planetary mill (RETS-CH PM 400) for about 10 min for subsequent sintering.

The resulting mixtures of the components were placed into a 30 mm diameter graphite mold and spark-plasma sintered (SPS, Summimoto, model SPS 825. CE, Dr. Sinter, Japan) under vacuum (6 Pa), pressing load of 85 MPa, soaking time of 3 – 4 min, temperature range of 1200 – 1600°C, and a heating rate of 100°C/min.

PROCEDURE FOR DETERMINING PROPERTIES OF OBTAINED POWDERS AND SINTERED SAMPLES

Phase composition, microstructure of synthesized powders and sintered samples, relative density (ρ_{rel}), linear shrinkage (Δl), modulus of elasticity (E), Vickers hardness (HV), and fracture toughness (K_{Ic}) were determined by the methods described in Ref. [5].

Theoretical density (ρ_{theor}), g/cm^3: mullite — 3.17; $(Ti_{0.6}Ta_{0.4})(C_{0.7}N_{0.3})$ — 8.2; B_4C — 5.2; *c*-BN — 3.49; α-, β-Ti, Nb, Cr/Zr — 4.76, 4.85/4.97, 5.06; α-, β-Ti,Cr,Zr — 4.9, 4,95; α-, β-Nb,Cr,Zr — 5.08, 5,18; α-, β-Ti,Nb,Cr,Zr — 6.23, 6.58; α-, β-Ti,Mo,Cr/V — 4.87, 4.95/5.08, 5.13; α-, β-Ti,Cr, V — 4.97, 5.08; α-, β-Mo,Cr,V — 5.13, 5.25; α-, β-Ti,Mo,Cr,V — 6.34, 6.73; α-, β-Mo,Nb,Cr — 4.70, 4.9; α-, β-Nb,Cr,Ta — 4.85, 4.97; α-, β-Mo,Cr,Ta — 4.95, 5.10; α-, β-Mo,Nb,Ta — 5.06, 5.13; α-, β-Mo,Nb,Cr,Ta — 6.12, 6.34.

In order to perform mathematical processing of the E and K_{Ic} data of the samples, the mean standard deviations from a certain number of values at a current temperature and the total values of standard deviations in the temperature range of 1200 – 1600°C were calculated using the following formula:

$$S_x = \sqrt{(\Sigma(n_i - n_{avr})^2)/n},$$

where S_x is the mean standard deviation; n_i is the result of the i-th measurement; n is the total number of measurements; and n_{avr} is the arithmetic mean of the results: $n_{avr} = (n_1 + n_2 + ... + n_i + ... + n_n)/n$, ($n$ = 5), where n_1, n_2, n_i, and n_n are the results of i-measurements.

TABLE 3. Proportions and initial component ratios*.

Parameter	Composition		
	M40($Ti_{0.6}Ta_{0.4}$)($C_{0.7}N_0$·3)5B_4C 5BN10Ti10Nb19,5Cr10,5Zr	M40($Ti_{0.6}Ta_{0.4}$)($C_{0.7}N_{0.3}$)5B_4C 5BN8,5Ti8,5Mo17Cr16V	M40($Ti_{0.6}Ta_{0.4}$)($C_{0.7}N_{0.3}$)5B_4C 5BN30Mo5Nb12,5Cr2,5Ta
Component mass, g per 100 g of mixture:			
40 mol.% ($Ti_{0.6}Ta_{0.4}$)($C_{0.7}N_{0.3}$) / 5 mol.% B_4C / 5 mol.% *h*-BN / 10 mol.% Ti / 10 mol.% Nb / 19.5 mol.% Cr / 10.5 mol.% Zr	54.62 / 3.11 / 1.44 / 5.76 / 11.16 / 12.16 / 11.75	—	—
40 mol.% ($Ti_{0.6}Ta_{0.4}$)($C_{0.7}N_{0.3}$) / 5 mol.% B_4C / 5 mol.% *h*-BN / 8.5 mol.% Ti / 8.5 mol.% Mo / 17 mol.% Cr / 16 mol.% V	—	57.65 / 3.28 / 1.52 / 5.16 / 10.33 / 11.18 / 10.88	—
40 mol.% ($Ti_{0.6}Ta_{0.4}$)($C_{0.7}N_{0.3}$) / 5 mol.% B_4C / 5 mol.% *h*-BN / 30 mol.% Mo / 5 mol.% Nb / 12.5 mol.% Cr / 2.5 mol.% Ta	—	—	48.55 / 2.76 / 1.28 / 30.72 / 4.95 / 6.92 / 4.82
Ratio:			
$3Al_2O_3$·$2SiO_2$ / ($Ti_{0.6}Ta_{0.4}$)($C_{0.7}N_{0.3}$) / B_4C / *h*-BN / Ti / Nb / Cr / Zr	1.83 / 32.15 / 69.44 / 17.36 /	—	—
$3Al_2O_3$·$2SiO_2$ / ($Ti_{0.6}Ta_{0.4}$)($C_{0.7}N_{0.3}$) / B_4C / *h*-BN / Ti / Mo / Cr / V	8.96 / 8.22 / 8.51		
$3Al_2O_3$·$2SiO_2$ / ($Ti_{0.6}Ta_{0.4}$)($C_{0.7}N_{0.3}$) / B_4C / *h*-BN / Mo / Nb / Cr / Ta	—	1.73 / 30.48 / 65.79 / 19.38 / 9.68 / 8.94 / 9.20	—
	—	—	2.06 / 36.23 / 78.12 / 3.25 / 20.2 / 14.45 / 20.7

* Component mass: $3Al_2O_3$/$2SiO_2$ 71.8/28.2 g per 100 g of mixture.

The total values of standard deviations were calculated using the following formula:

$$\Sigma S_x = S_{x1} + S_{x2} + \ldots + S_{xi} + \ldots + S_{xn},$$

where ΣS_x is the total value of standard deviation; S_{x1}, S_{x2}, S_{xi}, and S_{xn} are the standard deviations of each value at a current temperature.

RESULTS AND DISCUSSION

The phase composition of TiC, TiN, TaB_2, B_4C, and *h*-BN powders synthesized by the plasma-chemical method is shown in Fig. 1.

The phase composition of the synthesized TiC, TiN, B_4C, and *h*-BN powders is represented by narrow, intensive diffraction patterns of TiC, TiN, and B_4C, and less intensive, slightly wide diffraction patterns of TaB_2 (see Fig. 1). This is related with evoluted diffusion processes during solid-phase interaction of TiO_2 with C and TiO_2 with N_2, active dissolution of carbon powder/nitrogen in the low-temperature melt of B_2O_3 ($T_{melting}$ = 500°C) unlike less active solid-phase interaction of TaO_2 with B. In a result, more accelerated crystallization of TiC, TiN, B_4C, and *h*-BN phases, than TaB_2 phases.

Sintered (Ti,Ta)(C,N) material show crystalline, narrow, intensive diffraction patterns of ($Ti_{0.6}Ta_{0.4}$)($C_{0.7}N_{0.3}$) and weakly evoluted by-product crystalline phase $Ti_{1-(1-x)}B_2$ during the formation of solid solution of tantalum carbonitride (Fig. 2). The mechanisms of formation of tantalum carbonitride solid solutions are shown in the form of the following reactions:

$$\begin{aligned} &TiN_y + TiC_y + xTaB_2 \\ &\quad \rightarrow (Ti_{(1-x)}xTa^{4+})N_y + (Ti_{(1-x)}xTa^{4+})C_y + Ti_{1-(1-x)}B_2 \\ &\quad \rightarrow (Ti_{(1-x)}Ta)N_y + (Ti_{(1-x)}Ta)C_y + Ti_{1-(1-x)}B_2, \end{aligned} \quad (6)$$

$$\begin{aligned} &(Ti_{(1-x)}Ta)N_y + (Ti_{(1-x)}Ta)C_y + Ti_{1-(1-x)}B_2 \\ &\quad \rightarrow (Ti_{(1-x)}Ta{\cdot}Ta)C_{(y-1)}N_{(y+1)} \\ &\quad + (Ti_{(1-x)}Ta{\cdot}Ta)N_{(y-1)}C_{(y+1)} + Ti_{1-(1-x)}B_2 \\ &\quad \rightarrow (Ti_{(1-x)}2Ta)C_{(y-1)}N_{(y+1)} \\ &\quad + (Ti_{(1-x)}2Ta)N_{(y-1)}C_{(y+1)} + Ti_{1-(1-x)}B_2. \end{aligned} \quad (6.1)$$

The formation of ($Ti_{0.6}Ta_{0.4}$)($C_{0.7}N_{0.3}$) proceeds in several stages: formation of TiN and TiC melts, dissolution of TaB_2 in the TiN and TiC melts, and crystallization of ($Ti_{0.6}Ta_{0.4}$)($C_{0.7}N_{0.3}$). As the solubility of TaB_2 in the TiN and TiC melts increases and with the saturation of these melts with tantalum diboride, low-melting eutectics are formed in the triple TiC–TiN–TaB_2 system, and specifically in TaB_2–TiN at 2140 – 2185°C and TaB_2–TiC at 2190 – 2260°C. This corresponds to the region of limited solubility of the eutectic/peritectic composition of the TiN, TiC, and TaB_2 melts. The crystalline diffraction patterns of ($Ti_{0.6}Ta_{0.4}$)($C_{0.7}N_{0.3}$) are narrow and intensive. There are no

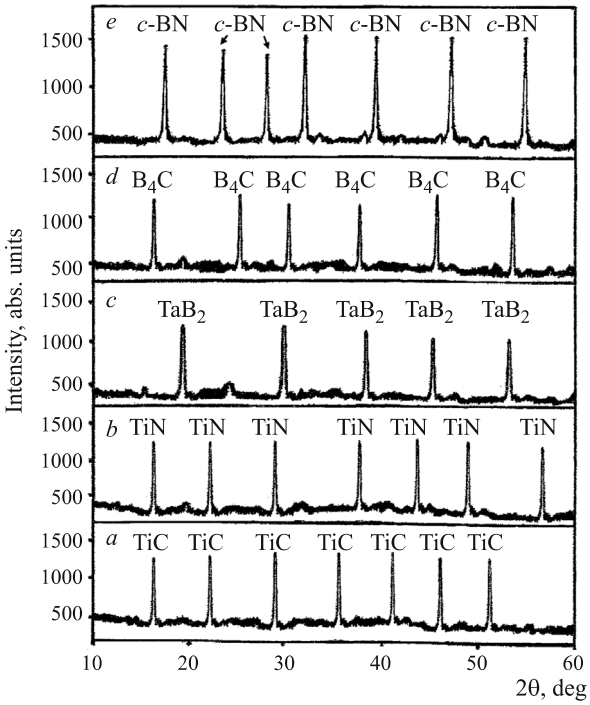

Fig. 1. Phase composition of TiC (*a*), TiN (*b*), TaB_2 (*c*), B_4C (*d*), and *h*-BN (*e*) powders synthesized by a plasma-chemical method at 1600°C.

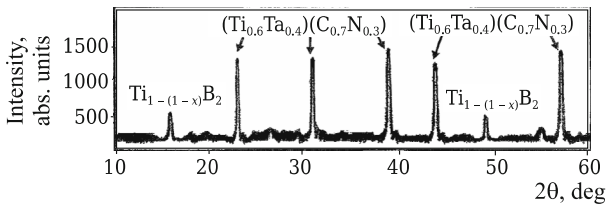

Fig. 2. Phase composition of (Ti,Ta)(C,N), obtained from TiC and TiN melts with an addition of TaB_2 and sintered in the temperature range of 2130 – 2280°C: $(Ti_{0.6}Ta_{0.4})(C_{0.7}N_{0.3})$ — solid solution of tantalum carbonitride; $Ti_{1–(1–x)}B_2$ — titanium diboride of a non-stoichiometric composition. The stoichiometry of $(Ti_{0.6}Ta_{0.4})(C_{0.7}N_{0.3})$ was determined based on the percentage content of Ti, Ta, C, and N in this compound with an error of ±2% by energy dispersive x-ray spectrometer (model JET-2300T).

eutectic/peritectic reactions between the TaB_2 melt and $(Ti_{0.6}Ta_{0.4})(C_{0.7}N_{0.3})$ particles in the low-melting eutectics of the ternary TiC–TiN–TaB_2 system. As a result, there is no recrystallization of the $(Ti_{0.6}Ta_{0.4})(C_{0.7}N_{0.3})$ phase and corresponding grains. These processes are similar to the processes occurring in a ternary equilibrium phase diagrams of TiC–TiN–TiB_2 of eutectic/hypereutectic composition at a pressing load of 5 MPa and above at 2327 – 2627°C [13]. As a result, evoluted diffusion and intercalation processes, as well as crystallization of tantalum carbonitride solid solution (see Fig. 2) unlike spark plasma sintering of Al_2O_3, SiO_2, TiC, and TiN mixtures via plastic state of TiC and TiN during unlimited dissolution, saturation of TiC and TiN, non-forming low-melting eutectics between themselves, or with Al_2O_3 and SiO_2, in a result don't contribute the crystallization of the Ti(C,N) phase due to the formation of an unlimited solubility region at a pressing load of 75 MPa and a temperature range of 1200 – 1600°C [14]. Crystallization of the (Ti,Ta)(C,N) phase as a single and stable (whole) compound indicates a region of complete solubility of TaB_2 in the TiN and TiC melts, and the lack of spinodal decomposition of (Ti,Ta)(C,N) compared to a ternary equilibrium phase diagram of TiC–TiN–TiB_2, of complete hypereu-tectic composition, which shows the region of incomplete TiB_2 solubility in the TiN and TiC melts, consisting of TiB_2 and melt [13]. In this sintering conditions, TaB_2 dissolution in the TiN and TiC melts is promoted with uniform, complete incorporation of the crystalline structures of intermediate solid solutions (see reactions (6) and (6.1)), and structuring of tantalum carbonitride solid solution, with a dense (cubic) structure. This method is more effective compared to obtaining Ti(C,N), including Ti(C,N) solid solution by using a mixture of TiC and TiN, a Ti(C,N) powder with a TaC or Ta additive in the solid phase, or with a TaC additive in Ni/Co melts during spark plasma sintering at a pressing load of 35, 30, or 50 MPa [15 – 18], since the absence of non-uniform, incomplete by-processes in the TiC and TiN melts typical for solid- or liquid-phase sintering.

The microstructure of sintered (Ti,Ta)(C,N) is crystalline, uniform, and densely sintered, with individual fine pores (Fig. 3*a*). This is related with evoluted diffusion and intercalation processes, as well as active crystallization of tantalum carbonitride solid solution (see Fig. 2) via low-melting eutectics in the region of limited solubility of eutectic/peritectic composition of the TiC, TiN, and TaB_2 melts of the TiC–TiN–TaB_2 triple system that promotes uniform and complete sintering of the (Ti,Ta)(C,N) particles. As a result, sintered grains of $(Ti_{0.6}Ta_{0.4})(C_{0.7}N_{0.3})$ are crystalline, monolithic, uniformly and densely packed, and partially fused with a small quantity of fine $Ti_{1–(1–x)}B_2$ grains, visible boundary areas of tetra-, hexa-, and octahedral shapes measuring 2 – 5 μm of size (see Fig. 3*b*). Due to uniform and complete incorporation reactions (see reaction (6.1)), uniform crystallization of (Ti,Ta)(C,N) (see Fig. 2), enhanced structuring and formation of a dense (Ti,Ta)(C,N) structure, the (Ti,Ta)(C,N) grains are hard.

The phase composition of the samples sintered from the initial components with different mixtures of metal powders by spark plasma sintering in the temperature range of 1200 – 1600°C is shown in Fig. 4*a*, *b*.

The mechanisms of formation of the crystalline quaternary solid solutions are complex and consist of different types of components interacting in the solid and liquid phases:

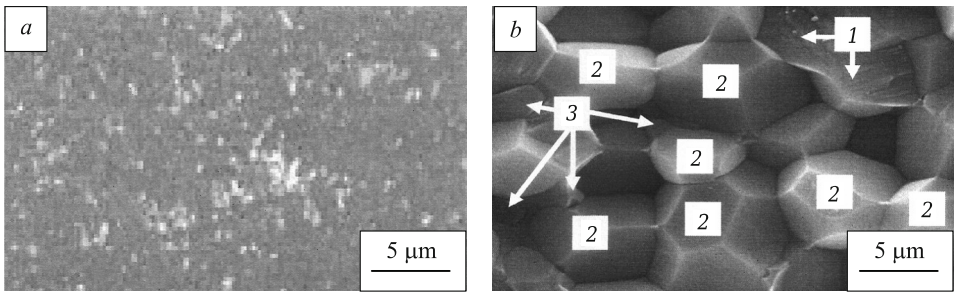

Fig. 3. Microstructure of (Ti,Ta)(C,N) sintered at 1500°C by a spark plasma sintering method: *a*) general microstructure; *b*) microstructure of sintered $(Ti_{0.6}Ta_{0.4})(C_{0.7}N_{0.3})$ grains; *1* — partially fused $(Ti_{0.6}Ta_{0.4})(C_{0.7}N_{0.3})$ grains; *2* — $(Ti_{0.6}Ta_{0.4})(C_{0.7}N_{0.3})$ grains of tetra-, hexα-, and octahedral shapes; *3* — $Ti_{1-(1-x)}B_2$ grains.

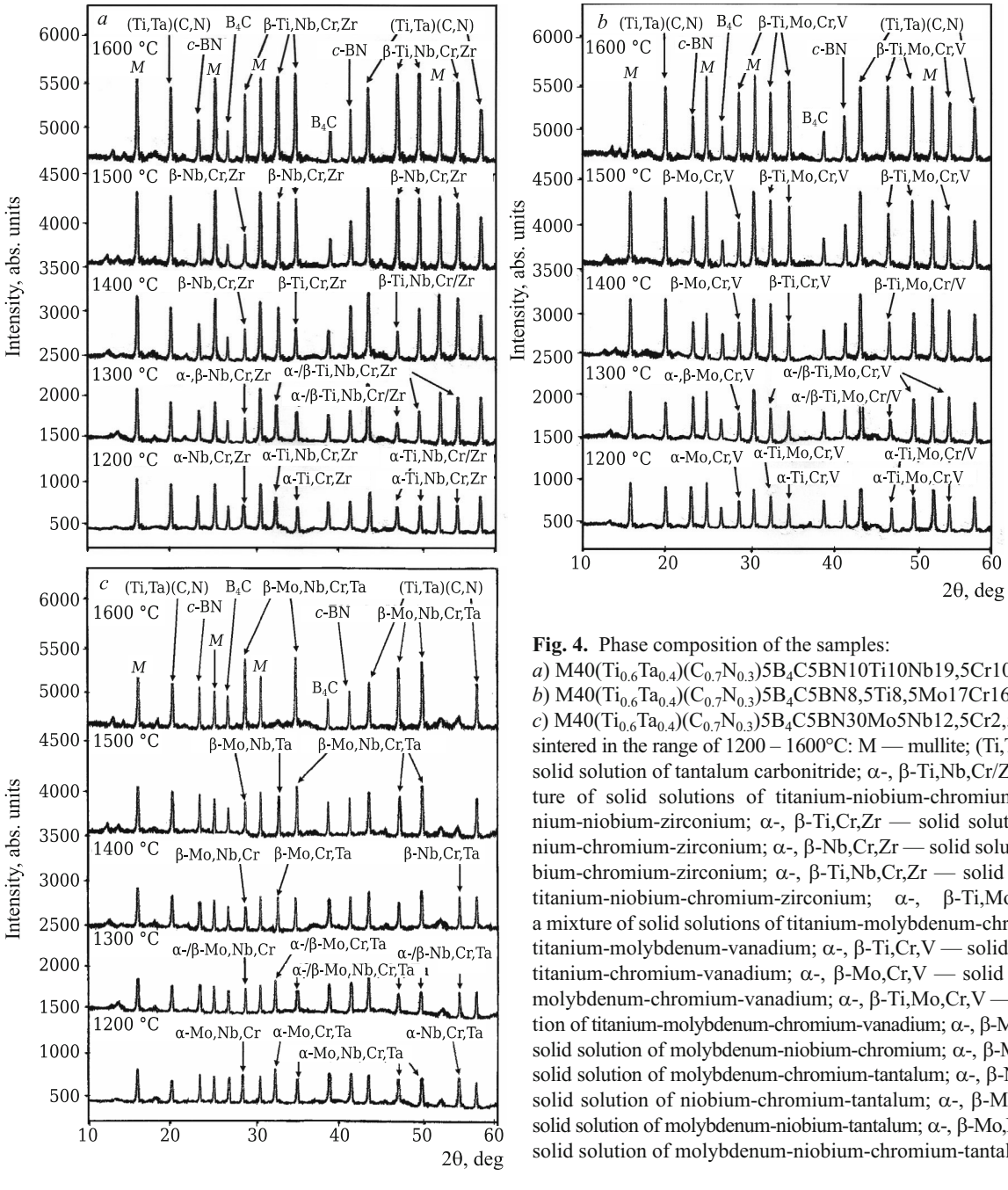

Fig. 4. Phase composition of the samples:
a) $M40(Ti_{0.6}Ta_{0.4})(C_{0.7}N_{0.3})5B_4C5BN10Ti10Nb19,5Cr10,5Zr$;
b) $M40(Ti_{0.6}Ta_{0.4})(C_{0.7}N_{0.3})5B_4C5BN8,5Ti8,5Mo17Cr16V$;
c) $M40(Ti_{0.6}Ta_{0.4})(C_{0.7}N_{0.3})5B_4C5BN30Mo5Nb12,5Cr2,5Ta$,
sintered in the range of 1200 – 1600°C: M — mullite; (Ti,Ta)(C,N) — solid solution of tantalum carbonitride; α-, β-Ti,Nb,Cr/Zr — a mixture of solid solutions of titanium-niobium-chromium and titanium-niobium-zirconium; α-, β-Ti,Cr,Zr — solid solution of titanium-chromium-zirconium; α-, β-Nb,Cr,Zr — solid solution of niobium-chromium-zirconium; α-, β-Ti,Nb,Cr,Zr — solid solution of titanium-niobium-chromium-zirconium; α-, β-Ti,Mo,Cr/V — a mixture of solid solutions of titanium-molybdenum-chromium and titanium-molybdenum-vanadium; α-, β-Ti,Cr,V — solid solution of titanium-chromium-vanadium; α-, β-Mo,Cr,V — solid solution of molybdenum-chromium-vanadium; α-, β-Ti,Mo,Cr,V — solid solution of titanium-molybdenum-chromium-vanadium; α-, β-Mo,Nb,Cr — solid solution of molybdenum-niobium-chromium; α-, β-Mo,Cr,Ta — solid solution of molybdenum-chromium-tantalum; α-, β-Nb,Cr,Ta — solid solution of niobium-chromium-tantalum; α-, β-Mo,Nb,Ta — solid solution of molybdenum-niobium-tantalum; α-, β-Mo,Nb,Cr,Ta — solid solution of molybdenum-niobium-chromium-tantalum.

Crystallization of α-, β-Ti, Nb, Cr, Zr:

– solid-phase reactions between chemical compounds and solid solutions:

$$\begin{aligned}&\alpha\text{-, }\beta\text{-(Ti,Cr)}_{\text{(nonstable.s.s.)}} + x\alpha\text{-, }\beta\text{-ZrCr}_{2\text{(solid phase)}}\\&+ x\alpha\text{-, }\beta\text{-NbCr}_{2\text{(solid phase)}} \rightarrow \alpha\text{-, }\beta\text{-(Ti}_{(1-x)}\text{,2}x\text{Cr}^{2+}\text{Cr)Nb}\\&+ \alpha\text{-, }\beta\text{-(Ti}_{(1-x)}\text{,2}x\text{Cr}^{2+}\text{Cr)Zr} + \alpha\text{-, }\beta\text{-(Ti}_{(1-x)}\text{, }x\text{Nb}^{4+}\text{Cr)2Cr}\\&+ \alpha\text{-, }\beta\text{-(Ti}_{(1-x)}\text{, }x\text{Zr}^{4+}\text{Cr)2Cr} + \alpha\text{-, }\beta\text{-(Ti,Cr}_{(1-\text{x})}x\text{Nb}^{4+}\text{)2Cr}\\&+ \alpha\text{-, }\beta\text{-(Ti,Cr}_{(1-\text{x})}\text{xZr}^{4+}\text{)2Cr}\\&\rightarrow \alpha\text{-, }\beta\text{-(Ti}_{(1-x)}\text{, 2}x\text{Cr·Cr)Nb} + \alpha\text{-, }\beta\text{-(Ti}_{(1-x)}\text{,2}x\text{Cr·Cr)Zr}\\&+ \alpha\text{-, }\beta\text{-(Ti}_{(1-x)}\text{, }x\text{Nb·Cr)2Cr}\\&+\alpha\text{-, }\beta\text{-(Ti}_{(1-x)}\text{,}x\text{Zr·Cr)2Cr} + \alpha\text{-, }\beta\text{-(Ti,Cr}_{(1-\text{x})}x\text{Nb)2Cr}\\&+ \alpha\text{-, }\beta\text{-(Ti,Cr}_{(1-\text{x})}x\text{Zr)2Cr}\\&\rightarrow \alpha\text{-, }\beta\text{-((Ti}_{(1-x)}\text{,2}x\text{Cr·Cr + Ti}_{(1-x)}\text{,2}x\text{Cr·Cr + Ti}_{(1-x)}\text{,}x\text{Nb·Cr}\\&+ \text{Ti}_{(1-x)}\text{, }x\text{Zr·Cr)Nb·Zr·2Cr·2Cr)}\\&+ \alpha\text{-, }\beta\text{-((Ti,Cr}_{(1-\text{x})}x\text{Nb + Ti,Cr}_{(1-\text{x})}x\text{Zr)2Cr·2Cr)}\\&\rightarrow \alpha\text{-, }\beta\text{-(2(Ti}_{(1-x)}\text{,4}x\text{Cr)·2Cr + 2Ti}_{(1-x)}\text{,}x\text{Nb}x\text{Zr·2Cr)Nb·Zr·4Cr}\\&+ \alpha\text{-, }\beta\text{-(2(Ti,Cr}_{(1-\text{x})}\text{)}x\text{Nb}x\text{Zr)4Cr} \rightarrow \alpha\text{-, }\beta\text{-(2Ti}_{(1-x)}\text{,4}x\text{Cr)·2Cr}\\&+ 2\text{Ti}_{(1-x)}\text{,}x\text{Nb,}x\text{Zr·2Cr)Nb·Zr·4Cr}\\&+ \alpha\text{-, }\beta\text{-(2Ti, 2Cr}_{(1-\text{x})}\text{,}x\text{Nb,}x\text{Zr)4Cr,}\end{aligned} \tag{7}$$

$$\begin{aligned}&\alpha\text{-, }\beta\text{-(Ti,Nb)}_{\text{(stable.s.s.)}} + x\alpha\text{-, }\beta\text{-ZrCr}_{2\text{(solid phase)}}\\&\rightarrow \alpha\text{-, }\beta\text{-(Ti}_{(1-x)}\text{,Nb2}x\text{Cr}^{2+}\text{)Zr} + \alpha\text{-, }\beta\text{-(Ti}_{(1-x)}\text{,Nb}x\text{Zr}^{4+}\text{)2Cr}\\&\rightarrow \alpha\text{-, }\beta\text{-(Ti}_{(1-x)}\text{,Nb2}x\text{Cr)Zr} + \alpha\text{-, }\beta\text{-(Ti}_{(1-x)}\text{,Nb}x\text{Zr)2Cr}\\&\rightarrow \alpha\text{-, }\beta\text{-((Ti}_{(1-x),}\text{Nb2}x\text{Cr + Ti}_{(1-x)}\text{,Nb}x\text{Zr)Zr·2Cr)}\\&\rightarrow \alpha\text{-, }\beta\text{-(2(Ti}_{(1-x)}\text{,Nb)2}x\text{Cr}x\text{Zr)Zr·2Cr}\\&\rightarrow \alpha\text{-, }\beta\text{-(2Ti}_{(1-x)}\text{,2Nb,2}x\text{Cr,}x\text{Zr)Zr·2Cr,}\end{aligned} \tag{8}$$

$$\begin{aligned}&\alpha\text{-, }\beta\text{-(Ti,Zr)}_{\text{(stable.s.s.)}} + x\alpha\text{-, }\beta\text{-NbCr}_{2\text{(solid phase)}}\\&\rightarrow \alpha\text{-, }\beta\text{-(Ti,Zr}_{(1-x\ )}x2\text{Cr}^{2+}\text{)Nb} + \alpha\text{-, }\beta\text{-(Ti,Zr}_{(1-x)}x\text{Nb}^{4+}\text{)2Cr}\\&\rightarrow \alpha\text{-, }\beta\text{-(Ti,Zr}_{(1-x)}2x\text{Cr)Nb} + \alpha\text{-, }\beta\text{-(Ti,Zr}_{(1-x)}x\text{Nb)2Cr}\\&\rightarrow \alpha\text{-, }\beta\text{-((Ti,Zr}_{(1-x)}2x\text{Cr + Ti, Zr}_{(1-x)}x\text{Nb)Nb·2Cr)}\\&\rightarrow \alpha\text{-, }\beta\text{-(2(Ti,Zr}_{(1-x)}\text{)2}x\text{Cr}x\text{Nb)Nb·2Cr}\\&\rightarrow \alpha\text{-, }\beta\text{-(2Ti,2Zr}_{(1-x)}\text{,2}x\text{Cr,}x\text{Nb)Nb·2Cr,}\end{aligned} \tag{9}$$

– solid-phase reactions between double solid solutions:

$$\begin{aligned}&\text{x}\alpha\text{-, }\beta\text{-(Zr,Nb)}_{\text{(relatively stable.s.s.)}} + y\alpha\text{-, }\beta\text{-(Ti,Cr)}_{\text{(nonstable.s.s.)}}\\&\rightarrow \alpha\text{-, }\beta\text{-(Zr}_{(1-y)}\text{, Nb}y\text{Cr}^{2+}\text{)Ti} + \alpha\text{-, }\beta\text{-(Zr}_{(1-y)}\text{,Nb}y\text{Ti}^{4+}\text{)Cr}\\&+ \alpha\text{-, }\beta\text{-(Zr,Nb}_{(1-y)}y\text{Cr}^{2+}\text{)Ti} + \alpha\text{-, }\beta\text{-(Zr,Nb}_{(1-y)}y\text{Ti}^{4+}\text{)Cr}\\&+ \alpha\text{, }\beta\text{-(Ti}_{(1-x)}\text{, Cr}x\text{Nb}^{4+}\text{)Zr} + \alpha\text{-, }\beta\text{-(Ti}_{(1-x)}\text{, Cr}x\text{Zr}^{4+}\text{)Nb}\\&+ \alpha\text{-, }\beta\text{-(Ti,Cr}_{(1-\text{x})}x\text{Nb}^{4+}\text{)Zr} + \alpha\text{-, }\beta\text{-(Ti,Cr}_{(1-x)}x\text{Zr}^{2+}\text{)Nb}\\&\rightarrow \alpha\text{-, }\beta\text{-(Zr}_{(1-y)}\text{,Nb}y\text{Cr)Ti} + \alpha\text{-, }\beta\text{-(Zr}_{(1-y)}\text{,Nb}y\text{Ti)Cr}\\&+ \alpha\text{-, }\beta\text{-(Zr,Nb}_{(1-y)}y\text{Cr)Ti} + \alpha\text{-, }\beta\text{-(Zr,Nb}_{(1-y)}y\text{Ti)Cr}\\&+ \alpha\text{-, }\beta\text{-(Ti}_{(1-x)}\text{,Cr}x\text{Nb)Zr} + \alpha\text{-, }\beta\text{-(Ti}_{(1-x)}\text{,Cr}x\text{Zr)Nb} + \alpha\text{-,}\\&\beta\text{-(Ti,Cr}_{(1-x)}x\text{Nb)Zr} + \alpha\text{-, }\beta\text{-(Ti,Cr}_{(1-x)}x\text{Zr)Nb} \rightarrow \alpha\text{-,}\\&\beta\text{-((Zr}_{(1-y)}\text{,Nb}y\text{Cr + Zr}_{(1-y)}\text{,Nb}y\text{Ti + Zr,Nb}_{(1-y)}y\text{Cr}\\&+ \text{Zr,Nb}_{(1-y)}y\text{Ti)Ti·Cr·Ti·Cr) + }\alpha\text{-, }\beta\text{-((Ti}_{(1-x)}\text{,Cr}x\text{Nb}\\&+ \text{Ti}_{(1-x)}\text{,Cr}x\text{Zr + Ti,Cr}_{(1-x)}x\text{Nb + Ti,Cr}_{(1-x)}x\text{Zr)Zr·Nb·Zr·Nb)}\\&\rightarrow \alpha\text{-, }\beta\text{-(2(Zr}_{(1-y)}\text{·Nb)}y\text{Cr}y\text{Ti + 2(Zr,Nb}_{(1-y)}\text{)}y\text{Cr}y\text{Ti)2Ti·2Cr}\\&+ \alpha\text{-, }\beta\text{-(2(Ti}_{(1-x)}\text{,Cr)}x\text{Nb}x\text{Zr + 2(Ti,Cr}_{(1-x)}\text{)}x\text{Nb}x\text{Zr)2Zr·2Nb}\\&\rightarrow \alpha\text{-, }\beta\text{-(2Zr}_{(1-y)}\text{·2Nb,}y\text{Cr,}y\text{Ti + 2Zr,2Nb}_{(1-y)}\text{,}y\text{Cr,}y\text{Ti)2Ti·2Cr}\end{aligned}$$

$$\begin{aligned}&+ \alpha\text{-, }\beta\text{-(2Ti}_{(1-x)}\text{,2Cr,}x\text{Nb,}x\text{Zr}\\&+ 2\text{Ti,2Cr}_{(1-x)}\text{,}x\text{Nb,}x\text{Zr)2Zr·2Nb,}\end{aligned} \tag{10}$$

$$\begin{aligned}&x\alpha\text{-, }\beta\text{-(Ti,Nb)}_{\text{(stable.s.s.)}} + y\alpha\text{-, }\beta\text{-(Cr,Zr)}_{\text{(stable.s.s.)}}\\&\rightarrow \alpha\text{-, }\beta\text{-(Ti}_{(1-y)}\text{,Nb}y\text{Cr}^{2+}\text{)Zr} + \alpha\text{-, }\beta\text{-(Cr,Zr}_{(1-x)}x\text{Nb}^{4+}\text{)Ti}\\&\rightarrow \alpha\text{-, }\beta\text{-(Ti}_{(1-y)}\text{,Nb}y\text{Cr)Zr} + \alpha\text{-, }\beta\text{-(Cr,Zr}_{(1-x)}x\text{Nb)Ti}\\&\rightarrow \alpha\text{-, }\beta\text{-(Ti}_{(1-y)}\text{,Nb,}y\text{Cr)Zr} + \alpha\text{-, }\beta\text{-(Cr,Zr}_{(1-x)}\text{,}x\text{Nb)Ti;}\end{aligned} \tag{11}$$

– liquid-phase reactions between chemical compounds, as well as chemical compounds and solid solutions:

$$\begin{aligned}&\gamma\text{-TiCr}_{2\text{(melt at 1320°C)}} + x\beta\text{-ZrCr}_{2\text{(solid phase)}} + x\beta\text{-NbCr}_{2\text{(solid phase)}}\\&\rightarrow \gamma\text{-(Ti}_{(1-x)}2x\text{Cr}^{2+}\text{Cr}_2\text{)Nb} + \gamma\text{-(Ti}_{(1-x)}2x\text{Cr}^{2+}\text{Cr}_2\text{)Zr}\\&+ \gamma\text{-(Ti}_{(1-x)}x\text{Nb}^{4+}\text{Cr}_2\text{)Cr}_2 + \gamma\text{-(Ti}_{(1-x)}x\text{Zr}^{4+}\text{Cr}_2\text{)Cr}_2\\&+ \gamma\text{-(TiCr}_{2(1-x)}x\text{Nb}^{4+}\text{)Cr}_2 + \gamma\text{-(TiCr}_{2(1-x)}x\text{Zr}^{4+}\text{)Cr}_2\\&\rightarrow \gamma\text{-(Ti}_{(1-x)}2x\text{Cr·Cr}_2\text{)Nb} + \gamma\text{-(Ti}_{(1-x)}2x\text{Cr·Cr}_2\text{)Zr}\\&+ \gamma\text{-(Ti}_{(1-x)}x\text{Nb·Cr}_2\text{)Cr}_2 + \gamma\text{-(Ti}_{(1-x)}x\text{Zr·Cr}_2\text{)Cr}_2\\&+ \gamma\text{-(TiCr}_{2(1-x)}x\text{Nb)Cr}_2 + \gamma\text{-(TiCr}_{2(1-x)}x\text{Zr)Cr}_2\\&\rightarrow \gamma\text{-((Ti}_{(1-x)}2x\text{Cr·Cr}_2 + \text{Ti}_{(1-x)}2x\text{Cr·Cr}_2 + \text{Ti}_{(1-x)}x\text{Nb·Cr}_2\\&+ \text{Ti}_{(1-x)}x\text{Zr·Cr}_2\text{)Nb·Zr·Cr}_2\text{·Cr}_2\text{) + }\gamma\text{-((TiCr}_{2(1-x)}x\text{Nb}\\&+ \text{TiCr}_{2(1-x)}x\text{Zr)Cr}_2\text{·Cr}_2\text{)} \rightarrow \gamma\text{-(2(Ti}_{(1-x)}2x\text{Cr)·2Cr}_2\\&+ 2\text{Ti}_{(1-x)}x\text{Nb}x\text{Zr·2Cr}_2\text{)Nb·Zr·2Cr}_2\\&+ \gamma\text{-(2TiCr}_{2(1-x)}x\text{Nb}x\text{Zr)2Cr}_2 \rightarrow\ \gamma\text{-(2Ti}_{(1-x)}\text{,4}x\text{Cr·2Cr}_2\\&+ 2\text{Ti}_{(1-x)}\text{,}x\text{Nb,}x\text{Zr·2Cr}_2\text{)Nb·Zr·2Cr}_2\\&+ \gamma\text{-(2TiCr}_{2(1-x)}\text{,}x\text{Nb,}x\text{Zr)2Cr}_2\text{,}\end{aligned} \tag{12}$$

$$\begin{aligned}&\gamma\text{-TiCr}_{2\text{(melt at 1320°C)}} + x\beta\text{-(Zr,Nb)}_{\text{(stable. s. s.)}}\\&\rightarrow \gamma\text{-(Ti}_{(1-x)}x\text{Nb}^{4+}\text{Cr}_2\text{)Zr} + \gamma\text{-(Ti}_{(1-x)}x\text{Zr}^{4+}\text{Cr}_2\text{)Nb}\\&+ \gamma\text{-(TiCr}_{2(1-x)}x\text{Nb}^{4+}\text{)Zr} + \gamma\text{-(TiCr}_{2(1-x)}x\text{Zr}^{4+}\text{)Nb}\\&\rightarrow \gamma\text{-(Ti}_{(1-x)}x\text{Nb·Cr}_2\text{)Zr} + \gamma\text{-(Ti}_{(1-x)}x\text{Zr·Cr}_2\text{)Nb}\\&+ \gamma\text{-(TiCr}_{2(1-x)}x\text{Nb)Zr} + \gamma\text{-(TiCr}_{2(1-x)}x\text{Zr)Nb}\\&\rightarrow \gamma\text{-((Ti}_{(1-x)}x\text{Nb·Cr}_2 + \text{Ti}_{(1-x)}x\text{Zr·Cr}_2\text{)Zr·Nb)}\\&+ \gamma\text{-((TiCr}_{2(1-x)}x\text{Nb + TiCr}_{2(1-x)}x\text{Zr)Zr·Nb)}\\&\rightarrow \gamma\text{-(2Ti}_{(1-x)}x\text{Nb}x\text{Zr·2Cr}_2\text{)Zr·Nb}\\&+ \gamma\text{-(2TiCr}_{2(1-x)}x\text{Nb}x\text{Zr)Zr·Nb}\\&\rightarrow \gamma\text{-(2Ti}_{(1-x)}\text{,}x\text{Nb,}x\text{Zr·2Cr}_2\text{)Zr·Nb}\\&+ \gamma\text{-(2TiCr}_{2(1-x)}\text{,}x\text{Nb,}x\text{Zr)Zr·Nb,}\end{aligned} \tag{13}$$

$$\begin{aligned}&\beta\text{-ZrCr}_{2\text{(melt at 1510°C)}} + x\beta\text{-(Ti,Nb)}_{\text{(stable.s.s.)}}\\&\rightarrow \gamma\text{-(Zr}_{(1-x)}x\text{Nb}^{4+}\text{Cr}_2\text{)Ti} + \gamma\text{-(Zr}_{(1-x)}\text{xTi}^{4+}\text{Cr}_2\text{)Nb}\\&+ \gamma\text{-(ZrCr}_{2(1-x)}x\text{Nb}^{4+}\text{)Ti} + \gamma\text{-(ZrCr}_{2(1-x)}x\text{Ti}^{4+}\text{)Nb}\\&\rightarrow \gamma\text{-(Zr}_{(1-x)}x\text{Nb·Cr}_2\text{)Ti +}\\&\gamma\text{-(Zr}_{(1-x)}x\text{Ti·Cr}_2\text{)Nb + }\gamma\text{-(ZrCr}_{2(1-x)}x\text{Nb)Ti}\\&+ \gamma\text{-(ZrCr}_{2(1-x)}x\text{Ti)Nb} \rightarrow \gamma\text{-((Zr}_{(1-x)}x\text{Nb·Cr}_2\\&+ \text{Zr}_{(1-x)}x\text{Ti·Cr}_2\text{)Ti·Nb)}\\&+ \gamma\text{-((ZrCr}_{2(1-x)}x\text{Nb + ZrCr}_{2(1-x)}x\text{Ti)Ti·Nb)}\\&\rightarrow \gamma\text{-(2Zr}_{(1-x)}x\text{Nb}x\text{Ti·2Cr}_2\text{)Ti·Nb}\\&+ \gamma\text{-(2ZrCr}_{2(1-x)}\text{,}x\text{Nb}x\text{Ti)Ti·Nb}\\&\rightarrow \gamma\text{-(2Zr}_{(1-x)}\text{,}x\text{Nb,}x\text{Ti·2Cr}_2\text{)Ti·Nb}\\&+ \gamma\text{-(2ZrCr}_{2(1-x)}\text{,}x\text{Nb,}x\text{Ti)Ti·Nb,}\end{aligned} \tag{14}$$

$\gamma\text{-}TiCr_{2(\text{melt at } 1320^\circ C)} + \beta\text{-}ZrCr_{2(\text{melt at } 1510^\circ C)}$
$+ x\beta\text{-}NbCr_{2(\text{solid phase})} \rightarrow \gamma\text{-}(Ti_{(1-x)}2xCr^{2+}Cr_2)Nb$
$+ \gamma\text{-}(Zr_{(1-x)}2xCr^{2+}Cr_2)Nb + \gamma\text{-}(Ti_{(1-x)}xNb^{4+}Cr_2)Cr_2$
$+ \gamma\text{-}(Zr_{(1-x)}xNb^{4+}Cr_2)Cr_2 + \gamma\text{-}(TiCr_{2(1-x)}xNb^{4+})Cr_2$
$+ \gamma\text{-}(ZrCr_{2(1-x)}xNb^{4+})Cr_2 \rightarrow \gamma\text{-}(Ti_{(1-x)}2xCr{\cdot}Cr_2)Nb$
$+ \gamma\text{-}(Zr_{(1-x)}2xCr{\cdot}Cr_2)Nb + \gamma\text{-}(Ti_{(1-x)}xNb{\cdot}Cr_2)Cr_2$
$+ \gamma\text{-}(Zr_{(1-x)}xNb{\cdot}Cr_2)Cr_2 + \gamma\text{-}(TiCr_{2(1-x)}xNb)Cr_2$
$+ \gamma\text{-}(ZrCr_{2(1-x)}xNb)Cr_2 \rightarrow \gamma\text{-}((Ti_{(1-x)}2xCr{\cdot}Cr_2$
$+ Zr_{(1-x)}2xCr{\cdot}Cr_2 + Ti_{(1-x)}xNb{\cdot}Cr_2$
$+ Zr_{(1-x)}xNb{\cdot}Cr_2)Nb{\cdot}Nb{\cdot}Cr_2{\cdot}Cr_2)$
$+ \gamma\text{-}((TiCr_{2(1-x)}xNb + ZrCr_{2(1-x)}xNb)Cr_2{\cdot}Cr_2)$
$\rightarrow \gamma\text{-}(2Ti_{(1-x)},2xCrxNb{\cdot}2Cr_2$
$+ 2Zr_{(1-x)},2xCrxNb{\cdot}2Cr_2)2Nb{\cdot}2Cr_2$
$+ \gamma\text{-}(TiCr_{2(1-x)}xNb + ZrCr_{2(1-x)}xNb)2Cr_2$
$\rightarrow \gamma\text{-}(2Ti_{(1-x)},2xCr,xNb{\cdot}2Cr_2$
$+ 2Zr_{(1-x)},2xCr,xNb{\cdot}2Cr_2)2Nb{\cdot}2Cr_2$
$+ \gamma\text{-}(TiCr_{2(1-x)},xNb + ZrCr_{2(1-x)},xNb)2Cr_2,$ (15)

Crystallization of α-, β-Ti, Mo, Cr, V:

– solid-phase reactions between double solid solutions:

$\alpha\text{-}, \beta\text{-}(Mo,V)_{(\text{stable.s.s.})} + x\alpha\text{-}, \beta\text{-}(Ti,Cr)_{(\text{nonstable.s.s.})}$
$\rightarrow \alpha\text{-}, \beta\text{-}(Mo_{(1-x)},VxCr^{2+})Ti + \alpha\text{-}, \beta\text{-}(Mo_{(1-x)},VxTi^{4+})Cr$
$+ \alpha\text{-}, \beta\text{-}(Mo,V_{(1-x)}xCr^{2+})Ti + \alpha\text{-}, \beta\text{-}(Mo,V_{(1-x)}xTi^{4+})Cr$
$\rightarrow \alpha\text{-}, \beta\text{-}(Mo_{(1-x),}VxCr)Ti + \alpha\text{-}, \beta\text{-}(Mo_{(1-x)},VxTi)Cr$
$+ \alpha\text{-}, \beta\text{-}(Mo,V_{(1-x)}xCr)Ti + \alpha\text{-}, \beta\text{-}(Mo,V_{(1-x)}xTi)Cr$
$\rightarrow \alpha\text{-}, \beta\text{-}((Mo_{(1-x),}VxCr + Mo_{(1-x),}VxTi + Mo,V_{(1-x)}xCr$
$+ Mo,V_{(1-x)}xTi)Ti{\cdot}Cr{\cdot}Ti{\cdot}Cr)$
$\rightarrow \alpha\text{-}, \beta\text{-}(2(Mo_{(1-x)},V)xCrxTi)Ti{\cdot}Cr$
$+ \alpha\text{-}, \beta\text{-}(2(Mo,V_{(1-x)})xCrxTi)Ti{\cdot}Cr$
$\rightarrow \alpha\text{-}, \beta\text{-}(2Mo_{(1-x)},2V,xCr,xTi)Ti{\cdot}Cr$
$+ \alpha\text{-}, \beta\text{-}(2Mo,2V_{(1-x)},xCr,xTi)Ti{\cdot}Cr,$ (16)

$\alpha\text{-}, \beta\text{-}(Ti, V)_{(\text{stable.s.s.})} + x\alpha\text{-}, \beta\text{-}(Cr,Mo)_{(\text{relatively stable.s.s.})}$
$\rightarrow \alpha\text{-}, \beta\text{-}(Ti_{(1-x)},VxCr^{2+})Mo + \alpha\text{-}, \beta\text{-}(Ti_{(1-x)},VxMo^{4+})Cr$
$\rightarrow \alpha\text{-}, \beta\text{-}(Ti_{(1-x)},VxCr)Mo + \alpha\text{-}, \beta\text{-}(Ti_{(1-x)},VxMo)Cr$
$\rightarrow \alpha\text{-}, \beta\text{-}((Ti_{(1-x)},VxCr + Ti_{(1-x)},VxMo)Mo{\cdot}Cr)$
$\rightarrow \alpha\text{-}, \beta\text{-}(2(Ti_{(1-x)},V)xCrxMo)Mo{\cdot}Cr$
$\rightarrow \alpha\text{-}, \beta\text{-}(2Ti_{(1-x)},2V,xCr,xMo)Mo{\cdot}Cr,$ (17)

$x\alpha\text{-}, \beta\text{-}(Ti, Mo)_{(\text{stable.s.s.})} + y\alpha\text{-}, \beta\text{-}(V,Cr)_{(\text{stable.s.s.})}$
$\rightarrow \alpha\text{-}, \beta\text{-}(Ti_{(1-y)},MoyCr^{2+})V + \alpha\text{-}, \beta\text{-}(V_{(1-x)},CrxMo^{4+})Ti$
$\rightarrow \alpha\text{-}, \beta\text{-}(Ti_{(1-y)}, MoyCr)V + \alpha\text{-}, \beta\text{-}(V_{(1-x)},CrxMo)Ti$
$\rightarrow \alpha\text{-}, \beta\text{-}((Ti_{(1-y)},MoyCr + V_{(1-x)},CrxMo)V{\cdot}Ti)$
$\rightarrow \alpha\text{-}, \beta\text{-}(Ti_{(1-y)},Mo,yCr)V + \alpha\text{-}, \beta\text{-}(V_{(1-x)}),Cr,xMo)Ti,$ (18)

– liquid-phase reaction between a chemical compound and solid solution:

$\gamma\text{-}TiCr_{2(\text{melt at } 1320^\circ C)} + x\beta\text{-}(Mo,V)_{(\text{stable.s.s.})}$
$\rightarrow \gamma\text{-}(Ti_{(1-x)}xV^{4+}Cr_2)Mo + \gamma\text{-}(Ti_{(1-x)}xMo^{4+}Cr_2)V$
$+ \gamma\text{-}(TiCr_{2(1-x)}xV^{4+})Mo + \gamma\text{-}(TiCr_{2(1-x)}xMo^{4+})V$
$\rightarrow \gamma\text{-}(Ti_{(1-x)}xV{\cdot}Cr_2)Mo + \gamma\text{-}(Ti_{(1-x)}xMo{\cdot}Cr_2)V$
$+ \gamma\text{-}(TiCr_{2(1-x)}xV)Mo + \gamma\text{-}(TiCr_{2(1-x)}xMo)V$
$\rightarrow \gamma\text{-}((Ti_{(1-x)}xV{\cdot}Cr_2 + Ti_{(1-x)}xMo{\cdot}Cr_2)Mo{\cdot}V)$
$+ \gamma\text{-}((TiCr_{2(1-x)}xV + TiCr_{2(1-x)}xMo)Mo{\cdot}V)$
$\rightarrow \gamma\text{-}(2Ti_{(1-x)}xVxMo{\cdot}2Cr_2)Mo{\cdot}V$
$+ \gamma\text{-}(2TiCr_{2(1-x)}xVxMo)Mo{\cdot}V)$
$\rightarrow \gamma\text{-}(2Ti_{(1-x)},xV,xMo{\cdot}2Cr_2)Mo{\cdot}V$
$+ \gamma\text{-}(2TiCr_{2(1-x)},xV,xMo)Mo{\cdot}V$ (19)

Crystallization of α-, β-Mo, Nb, Cr, Ta:

– solid-phase reactions between chemical compounds and solid solutions:

$\alpha\text{-}, \beta\text{-}(Cr,Mo)_{(\text{relatively stable.s.s.})} + x\alpha\text{-}, \beta\text{-}NbCr_{2(\text{solid phase})}$
$+ x\alpha\text{-}, \beta\text{-}TaCr_{2(\text{solid phase})} \rightarrow \alpha\text{-}, \beta\text{-}(Cr,Mo_{(1-x)}2xCr^{2+})Nb$
$+ \alpha\text{-}, \beta\text{-}(Cr,Mo_{(1-x)}2xCr^{2+})Ta + \alpha\text{-}, \beta\text{-}(Cr,Mo_{(1-x)}xNb^{4+})2Cr$
$+ \alpha\text{-}, \beta\text{-}(Cr,Mo_{(1-x)}xTa^{4+})2Cr \rightarrow \alpha\text{-}, \beta\text{-}(Cr,Mo_{(1-x)}2xCr)Nb$
$+ \alpha\text{-}, \beta\text{-}(Cr,Mo_{(1-x)}2xCr)Ta + \alpha\text{-}, \beta\text{-}(Cr,Mo_{(1-x)}xNb)2Cr$
$+ \alpha\text{-}, \beta\text{-}(Cr,Mo_{(1-x)}xTa)2Cr \rightarrow \alpha\text{-}, \beta\text{-}((Cr,Mo_{(1-x)}2xCr$
$+ Cr,Mo_{(1-x)}2xCr + Cr,Mo_{(1-x)}xNb$
$+ Cr,Mo_{(1-x)}xTa)Nb{\cdot}Ta{\cdot}2Cr{\cdot}2Cr)$
$\rightarrow \alpha\text{-}, \beta\text{-}(4(Cr,Mo_{(1-x)})4xCrxNbxTa)Nb{\cdot}Ta{\cdot}4Cr$
$\rightarrow \alpha\text{-}, \beta\text{-}(4Cr,4Mo_{(1-x)},4xCr,xNb,xTa)Nb{\cdot}Ta{\cdot}4Cr,$ (20)

$\alpha\text{-}, \beta\text{-}(Mo,Ta)_{(\text{stable.s.s.})} + x\alpha\text{-}, \beta\text{-}NbCr_{2(\text{solid phase})}$
$\rightarrow \alpha\text{-}, \beta\text{-}(Mo,Ta_{(1-x)}2xCr^{2+})Nb$
$+ \alpha\text{-}, \beta\text{-}(Mo,Ta_{(1-x)}xNb^{4+})2Cr$
$\rightarrow \alpha\text{-}, \beta\text{-}(Mo,Ta_{(1-x)}2xCr)Nb$
$+ \alpha\text{-}, \beta\text{-}(Mo,Ta_{(1-x)}xNb)2Cr$
$\rightarrow \alpha\text{-}, \beta\text{-}((Mo,Ta_{(1-x)}2xCr + Mo,Ta_{(1-x)}xNb)Nb{\cdot}2Cr)$
$\rightarrow \alpha\text{-}, \beta\text{-}(2(Mo,Ta_{(1-x)})2xCrxNb)Nb{\cdot}2Cr$
$\rightarrow \alpha\text{-}, \beta\text{-}(2Mo,2Ta_{(1-x)},2xCr,xNb)Nb{\cdot}2Cr,$ (21)

$\alpha\text{-}, \beta\text{-}(Mo,Nb)_{(\text{solid phase})} + x\alpha\text{-}, \beta\text{-}TaCr_{2(\text{solid phase})}$
$\rightarrow \alpha\text{-}, \beta\text{-}(Mo,Nb_{(1-x)}2xCr^{2+})Ta$
$+ \alpha\text{-}, \beta\text{-}(Mo,Nb_{(1-x)}xTa^{4+})2Cr$
$\rightarrow \alpha\text{-}, \beta\text{-}(Mo,Nb_{(1-x)}2xCr)Ta + \alpha\text{-}, \beta\text{-}(Mo,Nb_{(1-x)}xTa)2Cr$
$\rightarrow \alpha\text{-}, \beta\text{-}((Mo,Nb_{(1-x)}2xCr + Mo,Nb_{(1-x)}xTa)Ta{\cdot}2Cr)$
$\rightarrow \alpha\text{-}, \beta\text{-}(2(Mo,Nb_{(1-x)})2xCrxTa)Ta{\cdot}2Cr$
$\rightarrow \alpha\text{-}, \beta\text{-}(2Mo,2Nb_{(1-x)},2xCr,xTa)Ta{\cdot}2Cr,$ (22)

– solid-phase reactions between double solid solutions:

$\alpha\text{-}, \beta\text{-}(Nb,Ta)_{(\text{stable.s.s.})} + x\alpha\text{-}, \beta\text{-}(Cr,Mo)_{(\text{relatively stable.s.s.})}$
$\rightarrow \alpha\text{-}, \beta\text{-}(Nb,Ta_{(1-x)}xCr^{2+})Mo + \alpha\text{-}, \beta\text{-}(Nb,Ta_{(1-x)}xMo^{4+})Cr$
$\rightarrow \alpha\text{-}, \beta\text{-}(Nb,Ta_{(1-x)}xCr)Mo + \alpha\text{-}, \beta\text{-}(Nb,Ta_{(1-x)}xMo)Cr$
$\rightarrow \alpha\text{-}, \beta\text{-}((Nb,Ta_{(1-x)}xCr + Nb,Ta_{(1-x)}xMo)Mo{\cdot}Cr)$
$\rightarrow \alpha\text{-}, \beta\text{-}(2(Nb,Ta_{(1-x)})xCrxMo)Mo{\cdot}Cr$
$\rightarrow \alpha\text{-}, \beta\text{-}(2Nb,2Ta_{(1-x)},xCr,xMo)Mo{\cdot}Cr.$ (23)

Samples with mixtures of metal powders show more intensive mullitization and crystallization of (Ti,Ta)(C,N) compared to crystallization of the B_4C and *c*-BN phases (see

Fig. 4*a* – *c*) in the temperature range of 1200 – 1600°C. Higher crystallization of mullite, (Ti,Ta) (C,N) with a dense (cubic) structure, and partially of B_4C and *c*-BN above 1400°C (see Fig. 4*a*, *b*) is associated with the formation of stoichiometric compositions and complete structuring of these crystalline phases via low-melting eutectics in the mixtures of Ti, Nb, Cr, Zr and Ti, Mo, Cr, V (see reactions (12) – (15), (19)), unlike less active processes during crystallization of mullite (Ti,Ta)(C,N), B_4C, and *c*-BN (see Fig. 4*c*) during eutectoid reactions in the mixture of Mo,Nb, Cr, and Ta (see reactions (20) – (23)). The mechanisms of development of these crystalline phases are associated with the dissolution of Al_2O_3 and SiO_2 in the melts (eutectics) and eutectoid mixtures, oxidation of metallic and non-oxide components, formation of their oxide compounds, low-melting/eutectoid compounds between oxide components of metallic powders and Al_2O_3 and SiO_2, as well as between oxide components of metallic powders and non-oxide compounds. The formation of less crystalline phases, such as B_4C and *c*-BN is caused by the low content of the resulting B_2O_3 at 5 mol.% B_4C and BN in the sintered compositions, which reduces the completeness and activity of the formation of low-melting/eutectoid compounds between the oxide components of metallic powders and B_2O_3. There is no *c*-BN → *h*-BN phase transformation in the samples. This is related with differently uniform structuring and the formation of stable, various dense crystalline structures (e.g., (Ti,Ta)(C,N); B_4C; β-Ti, Nb, Cr, Zr; β-Ti, Mo, Cr, V; β-Mo,Nb, Cr, Ta), which contributes the strengthening and reinforcing of the *c*-BN phase crystalline structure. This results in a more complete, uniform structuring and visible higher ingrowth of the *c*-BN crystalline phase compared to crystalline B_4C. The samples contain no reaction products (e.g., non-oxide crystalline phases) as a result of interaction between crystalline (Ti,Ta)(C,N), B_4C, and *c*-BN phases due to their dense structures and low reaction ability. The samples show narrow and different intensity peaks of the crystalline phases α-; β-Ti, Nb, Cr, Zr; α-, β-Ti, Mo, Cr, V; α-, β-Mo,Nb, Cr, Ta in the temperature range of 1200 – 1600°C (see Fig. 4*a* – c). Thus, up to 1400°C, the crystalline phase of α-Ti, Mo, Cr, V is more evoluted than crystalline phases of α-Ti, Nb, Cr, Zr and α-, β-Mo,Nb, Cr, Ta. This is related with active diffusion and uniform, complete intercalation of small and roughly equal sizes of cations Cr^{2+}, V^{4+}, Mo^{4+}, and Ti^{4+} compared to limited diffusion and gradual, heterogeneous incorporation of different size of cations (e.g., Cr^{2+}, Nb^{4+}, Ti^{4+}, Zr^{4+} and Cr^{2+}, Mo^{4+}, Nb^{4+}, Ta^{4+}) into the structures of binary solid solutions in solid phases (see reactions (7) – (11), (16) – (18), and (20) – (23)). The crystalline phase of α-Ti,Mo,Cr,V is more structured with a dense structure than the α-Ti,Nb,Cr,Zr and α-Mo,Nb,Cr,Ta crystalline phases up to 1400°C. Above 1400°C, a higher ingrowth of the β-Ti,Nb,Cr,Zr crystalline phase is observed compared to the β-Ti,Mo,Cr,V and β-Mo,Nb,Cr, Ta crystalline phases. This is explained by a higher diffusion with relatively uniform and complete incorporation of different size of cations (e.g., Cr^{2+}, Nb^{4+}, Ti^{4+}, and Zr^{4+}) into the structures of binary solid solutions via a subsequent dissolution of the binary solid solutions and formation of low-melting eutectics of various compositions in the primary melt (γ-$TiCr_2$) at 1320°C (see reactions (12), (13)), secondary melt (β-$ZrCr_2$) at 1560°C (see reaction (14)), and in the relatively stable low-melting composition of γ-$TiCr_2$ and β-$ZrCr_2$ melts with solid particles of β-$NbCr_2$ in the region of partially limited solubility of β-$NbCr_2$ in these melts in the temperature range of 1560 – 1600°C (see reaction (15)), which promotes the diffusion and intercalation processes. This is different from a less active diffusion with the develop-ment of uniform and complete incorporation of small and about equal size of cations Cr^{2+}, V^{4+}, Mo^{4+}, and Ti^{4+} into the structures of binary solid solutions via a one-stage dissolution of binary solid solutions and formation of a low-melting eutectics in a single melt of γ-$TiCr_2$ in the temperature range of 1320 – 1600°C (see reaction (19)), as well as a limited diffusion and gradual, heterogeneous solid-phase incorporation of different size of cations Cr^{2+}, Mo^{4+}, Nb^{4+}, and Ta^{4+} into the binary solid solution structures via a solid-phase dissolution of α-, β-$NbCr_2$, and α-, β-$TaCr_2$ of various density, in the stable and dense binary solid solution structures and solid-phase incorporation of stable and dense binary solid solutions in the wide and uniform region of complete solubility of the metal components (see reactions (20) – (23)). The region of partially limited solubility of β-$NbCr_2$ in γ-$TiCr_2$ and β-$ZrCr_2$ melts is associated with a different content of β-$NbCr_2$ dissolved in the corresponding melts ($TiCr_2$ and $ZrCr_2$) in the 240°C melting point range of the components and a narrow 1560 – 1600°C temperature range of the formation of this region, which does not contribute to a complete dissolution of β-$NbCr_2$ in the $ZrCr_2$ melt in the composition, containing a mixture of Ti, Nb, Cr, and Zr powders. As a result, the β-Ti,Mo,Cr,V crystalline phase is more structured with a dense structure than the β-Ti,Nb,Cr,Zr and β-Mo,Nb,Cr,Ta crystalline phases with less dense structures in the temperature range of 1400 – 1600°C. The feature of solid-phase crystallization and the stability of the α-, β-Mo,Nb,Cr,Ta phase are associated with the gradual, uniform, and complete intercalation of a larger Ta^{4+} cation into the structures of binary solid solutions with low diffusion of Ta^{4+} cation and more dense structure of Ta at a low tantalum content in the initial component mixture (see Table 3) via reactions (20) and (22), unlike liquid-phase crystallization of the β-Ti,Nb,Cr,Zr and β-Ti,Mo,Cr,V phases, where the incorporation of large-size Ti^{4+} and Zr^{4+} cations into the structures of binary solid solutions is promoted via low-melting eutectics. In a result increase structuring and the density of the structures of α-, β-Mo,Nb,Cr,Ta crystalline phases.

However, the compositions of α-, β-Ti,Mo,Cr,V crystalline phases display more intensive crystalline phases of ter-

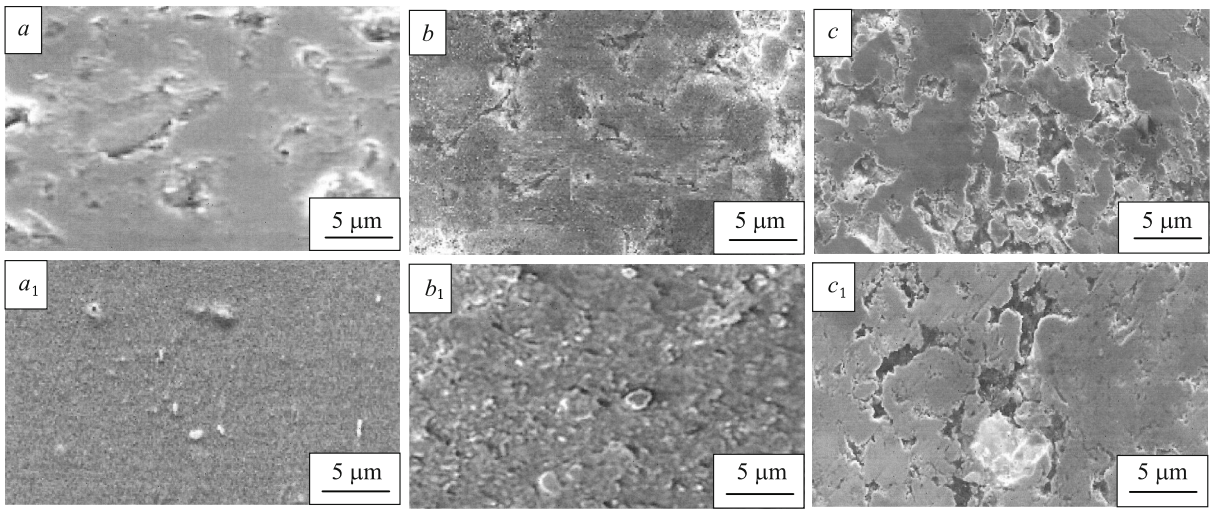

Fig. 5. Microstructures of samples sintered from the compositions: M40($Ti_{0.6}Ta_{0.4}$)($C_{0.7}N_{0.3}$)5B_4C5BN10Ti10Nb19,5Cr10,5Zr (*a*, a_1); M40($Ti_{0.6}Ta_{0.4}$)($C_{0.7}N_{0.3}$)5B_4C5BN8,5Ti8,5Mo17Cr16V (*b*, b_1); M40($Ti_{0.6}Ta_{0.4}$)($C_{0.7}N_{0.3}$)5B_4C5BN30Mo5Nb12,5Cr2,5Ta (*c*, c_1) at 1300°C (*a*, *b*, *c*) and 1500°C (a_1, b_1, c_1).

nary solid solutions compared to less intense crystalline phases of ternary solid solutions in the compositions of α-, β-Ti,Nb,Cr,Zr and α-, β-Mo,Nb,Cr,Ta crystalline phases in the temperature range 1200 – 1400°C. Higher crystallization of ternary solid solution phases is associated with active diffusion and uniform, complete solid-phase incorporation of small and about equally size of cations (e.g., Cr^{2+}, V^{4+}, Ti^{4+}, Mo^{4+}) into the α-, β-(Ti,Cr); α-, β-(Mo,V); α-, β-(Ti,V); α-, β-(Cr,Mo); α-, β-(Ti,Mo); and α-, β-(V,Cr) structures (see reactions (16) – (18)), but less active crystallization of ternary solid solution phases is caused by limited diffusion and gradual, inhomogeneous solid-phase incorporation of different size of cations (e.g., Cr^{2+}, Nb^{4+}, Ti^{4+}, Zr^{4+}) into the α-, β-(Ti,Cr); α-, β-(Ti,Nb); α-, β-(Ti,Zr); α-, β-(Zr,Nb); and α-, β-(Cr,Zr) structures (see reactions (7) – (11)), as well as different size cations (e.g., Cr^{2+}, Mo^{4+}, Nb^{4+}, Ta^{4+}) into the α-, β-(Mo,Ta); α-, β-(Mo,Nb); α-, β-(Nb,Ta); and α-, β-(Cr,Mo) structures (see reactions (20) – (23)). As a result, crystalline phases of the ternary solid solutions of composition with Ti, Mo, Cr, and V powders are more structured with dense structures, than the crystalline phases of ternary the solid solutions of compositions with Ti, Nb, Cr, Zr and Mo,Nb, Cr, Ta powders with less dense structures in the temperature range of 1200 – 1400°C. However, at 1500°C, a different crystallization of more dense structures of ternary solid solutions, such as β-Nb,Cr,Zr; β-Mo,Cr,V; and β-Mo,Nb,Ta are visible (see Fig. 4). This is related with different activity and homogeneity of incorporation of the various dense structures of metallic components. The structures of crystalline phases, such as α-, β-Ti,Nb,Cr,Zr; α-, β-Ti,Mo,Cr,V; and α-, β-Mo,Nb,Cr,Ta, are more dense compared to the structures of ternary solid solutions of such compositions, since the α-, β-Ti,Nb,Cr,Zr; α-, β-Ti,Mo,Cr,V; and α-, β-Mo,Nb,Cr,Ta crystalline phases — solid solutions of complete incorporation of metallic components. Above 1500°C, crystallizes only β-Ti,Nb,Cr,Zr; β-Ti,Mo,Cr,V; and β-Mo,Nb,Cr,Ta phases. This is corresponds the region of complete liquid-/solid-phase solubility of the quaternary equilibrium phase diagrams Ti–Nb–Cr–Zr, Ti–Mo–Cr–V, and Mo–Nb–Cr–Ta [10 – 12]. Crystalline phases, such as α-, β-Ti,Nb,Cr,Zr; α-, β-Ti,Mo,Cr,V; and α-, β-Mo,Nb,Cr,Ta are present as single solid solutions without decomposition into constituent components. This indicates the absence of spinodal decomposition of these solid solutions. In the temperature range of 1200 – 1600°C, the samples contain no chemical com-pounds of the following compositions: Ti*x*Nb*y*Cr_zZr_m, Ti*x*Mo*y*Cr_zV_m, or Mo*x*Nb*y*Cr_zTa_m. This is related with a high effect of the pressing load (85 MPa), which promotes various types, uniformity and intensity of the solid- and liquid-phase incorporation reactions (see reactions (7) – (23)), and phase transformations: α- → β-Ti,Nb,Cr,Zr; α- → β-Ti,Mo,Cr,V; and α- → β-Mo,Nb,Cr,Ta.

The microstructures of plasma-sintered samples at 1300 and 1500°C are shown in Fig. 5.

At 1300°C, the microstructures of the samples with mixtures of metal powders, are crystalline, different-uniform, variously dense sintered with containing different sizes of pores, in particular separate large pores in the sample with a mixture of Ti, Nb, Cr, and Zr powders (see Fig. 5*a*), some small pores in the sample with a mixture of Ti, Mo, Cr, and V powders (see Fig. 5*b*), and more quantity of different sizes of pores between weakly sintered particles in the sample with a mixture of Mo, Nb, Cr, and Ta powders (see Fig. 5*c*). This is related with a difference of reaction mechanisms, intensity and homogeneity of incorporation of different size metal cations into the structures of binary solid solutions (see reactions (7) – (11), (16) – (18), (20) – (23)), solid phase struc-

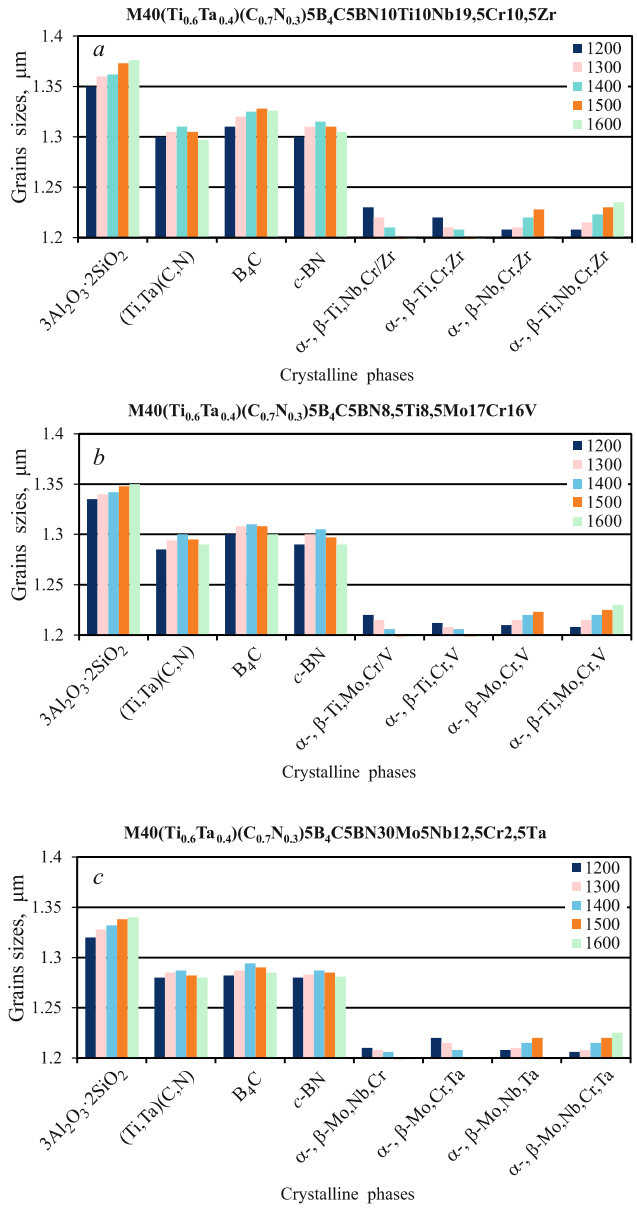

Fig. 6. Size distribution of the grains of crystalline phases of the samples:
a) M40($Ti_{0.6}Ta_{0.4}$)($C_{0.7}N_{0.3}$)5B_4C5BN10Ti10Nb19,5Cr10,5Zr;
b) M40($Ti_{0.6}Ta_{0.4}$)($C_{0.7}N_{0.3}$)5B_4C5BN8,5Ti8,5Mo17Cr16V;
c) M40($Ti_{0.6}Ta_{0.4}$)($C_{0.7}N_{0.3}$)5B_4C5BN30Mo5Nb12,5Cr2,5Ta,
sintered in the range of 1200 – 1600°C: ■) 1200°C; ■) 1300°C; ■) 1400°C; ■) 1500°C; ■) 1600°C.

turing of the crystalline phases (Ti,Ta) (C,N); B_4C; *c*-BN; α-Ti,Nb,Cr,Zr; α-Ti,Mo,Cr,V; and α-Mo,Nb,Cr,Ta (see Fig. 4*a* – *c*). This variously affects the density of crystalline phases, uniformity and completeness of solid-phase sintering of the ceramic particles, ceramic particles and particles of solid solutions of metallic phases, particles of ternary and quaternary solid solutions of metallic phases of different density, as well as pore filling due to various-intensive diffusion processes, at the boundaries of these particles at 1300°C in compositions with a mixtures of Ti, Mo, Cr, V; Ti, Nb, Cr, Zr; and Mo, Nb, Cr, and Ta powders.

A more uniform and densely sintered microstructure with the absent of pores is visible in the sample with a mixture of Ti, Nb, Cr, and Zr powders (see Fig. 5a_1), unlike non-uniformly sintered micro-structure, consisting of uniform, dense, and partially layered crystalline regions in the form of various-dense and various-size layering areas, containing small pores at 1500°C (see Fig. 5b_1), as well as unevenly sintered microstructure with coarse pores at 1500°C (see Fig. 5b_1). The sample with a mixture of Ti, Mo, Cr, and V powders shows a clear boundary between such crystalline regions (see Fig. 5b_1). The uniform and densely sintered crystalline region is explained by a homogeneous, active sintering of various-dense particles of (Ti,Ta)(C,N), B_4C, *c*-BN and β-Mo,Cr,V, as well as β-Ti,Mo,Cr,V, but a partially layered crystalline region is caused by inhomogeneous and gradual sintering of equally dense ceramic and β-Ti,Mo,Cr,V particles. The differences in diffusion processes in each of the crystalline regions cause uneven and incomplete sintering at the joints of various-dense crystalline regions, thus forming a boundary section. The differences in sample microstructures at 1500°C are associated with different reaction mechanisms of liquid-/solid-phase crystallization of β-Ti,Nb,Cr,Zr; β-Ti,Mo,Cr,V; and β-Mo,Nb,Cr,Ta (see reactions (12) – (15), (19), (20) – (23) and see Fig. 4*a* – *c*), activity, homogeneity, and completeness of incorporation of various-dense structures of the metallic compo-nents, structuring of crystalline phases, such as (Ti,Ta)(C,N); B_4C; *c*-BN; β-Ti,Nb,Cr,Zr; β-Ti,Mo,Cr,V; and β-Mo,Nb,Cr,Ta (see Fig. 4*a* – *c*) via low-melting eutectics and eutectoid, different compositions of the low-melting eutectic and eutectoid. This differently affects the uniformity and completeness of sintering of ceramic particles, ceramic particles and particles of solid solutions of metallic phases, pore filling, as well as the activity and uniformity of sintering, density, uniformity, width, and path of the boundary layers of β-Nb,Cr,Zr; β-Mo,Cr,V; β-Mo,Nb,Ta between heterogeneous particles, as well as the uniformity and completeness of sintering such boundary layers with ceramic particles and particles of solid solutions of metallic phases in the temperature range of 1400 – 1600°C with a pressing load of 85 MPa.

The distribution of crystalline phase grains sizes, relative density (ρ_{rel}), and linear shrinkage (Δl) in the temperature range of 1200 – 1600°C, as well as the boundary microstructures of ceramic (oxide, non-oxide) and metallic crystalline phases at 1500°C, photo of the indentation press at 1300 and 1500°C, microcracks propagation paths across the boundary layers, physico-mechanical properties in the temperature range of 1200 – 1600°C of the samples with different mixtures of metal powders, are shown in Figs. 6 – 20.

An increase in ρ_{rel} and Δl of the samples with mixtures of metal powders, occurs gradually up to 1400°C and more actively from 1400 to 1600°C. In particular, the sample, containing a mixture of Ti, Nb, Cr, and Zr powders, shows

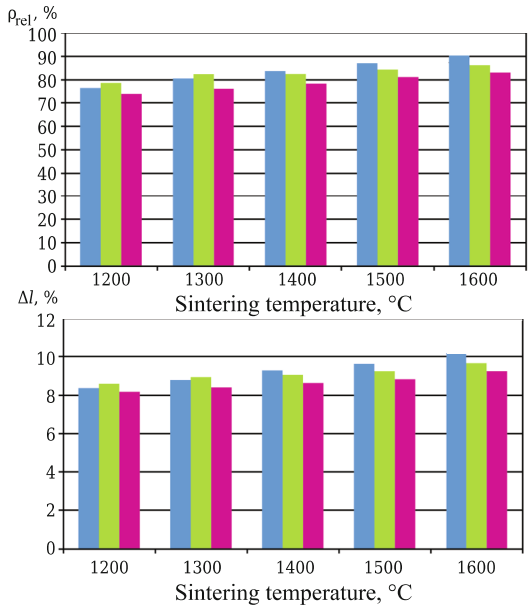

Fig. 7. Variation in ρ_{rel} (*a*) and Δl (*b*) of the samples: M40$(Ti_{0.6}Ta_{0.4})(C_{0.7}N_{0.3})5B_4$C5BN10Ti10Nb19,5Cr10.5Zr (■); *M40*$(Ti_{0.6}Ta_{0.4})(C_{0.7}N_{0.3})5B_4$C5BN8,5Ti8,5Mo17Cr16V (■); *M40*$(Ti_{0.6}Ta_{0.4})(C_{0.7}N_{0.3})5B_4$C5BN30Mo5Nb12,5Cr2,5Ta (■), sintered in the range of 1200 – 1600°C.

higher ingrowth of sintering compared to the samples, containing mixtures of Ti, Mo, Cr, V and Mo, Nb, Cr, Ta powders, in the temperature range of 1400 – 1600°C. A gradual sintering up to 1400°C is caused by a gradual intercalation processes at similar solid-phase reaction mechanisms of crystallization of quaternary solid solutions of metallic phases (see reactions (7) – (11), (16) – (18), (20) – (23)), solid-phase structuring of crystalline phases in the temperature range of 1200 – 1400°C (see Fig. 4*a* – *c*), uneven and incomplete diffusion processes with inhomogeneous solid-phase sintering of ceramic particles, ceramic particles and particles of solid solutions of metallic phases with the formation corresponding microstructures (see Fig. 5*a* – *c*), and low effect of variously-dispersed particles (see Fig. 6) on solid-phase sintering. The active sintering above 1400°C is associated with the evolution of intercalation processes at different reaction mechanisms of conversion of binary to quaternary solid solutions of metallic phases (see reactions (12) – (15), (19), (20) – (23)), liquid-/solid-phase crystallization of quaternary solid solutions of metallic phases (see Fig. 4*a* – *c*), uniform and complete diffusion processes via low-melting eutectics and eutectoid, homogeneity and completeness of sintering of the compositions with the formation more densely sintered microstructures (see Fig. 5a_1 – c_1), and higher effect of variously-dispersed particles (see Fig. 6) on liquid-/solid-phase sintering.

Development of physico-mechanical properties of the samples, containing different mixtures of metal powders differs from sintering the compositions in the temperature range of 1200 – 1600°C. A higher increase in *E*, K_{Ic}, and *HV* is

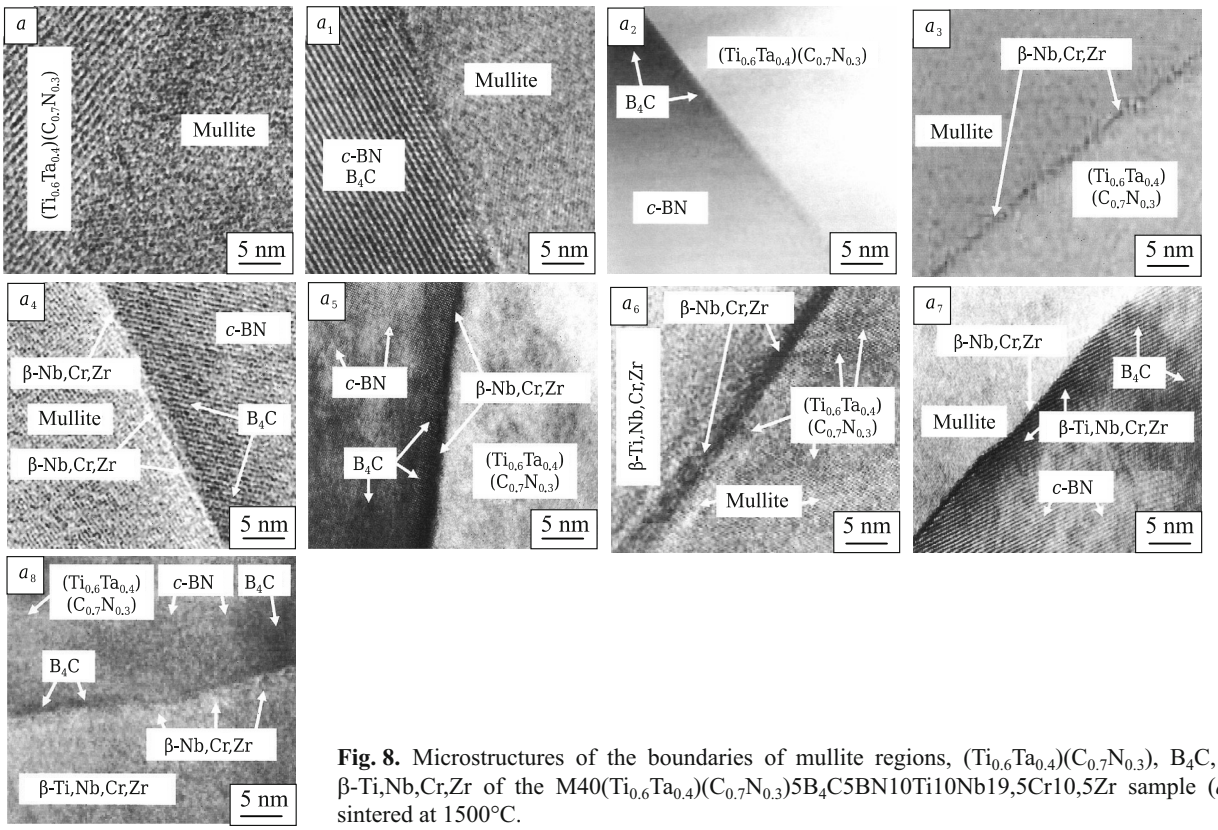

Fig. 8. Microstructures of the boundaries of mullite regions, $(Ti_{0.6}Ta_{0.4})(C_{0.7}N_{0.3})$, B_4C, *c*-BN, β-Ti,Nb,Cr,Zr of the M40$(Ti_{0.6}Ta_{0.4})(C_{0.7}N_{0.3})5B_4$C5BN10Ti10Nb19,5Cr10,5Zr sample (a – a_8), sintered at 1500°C.

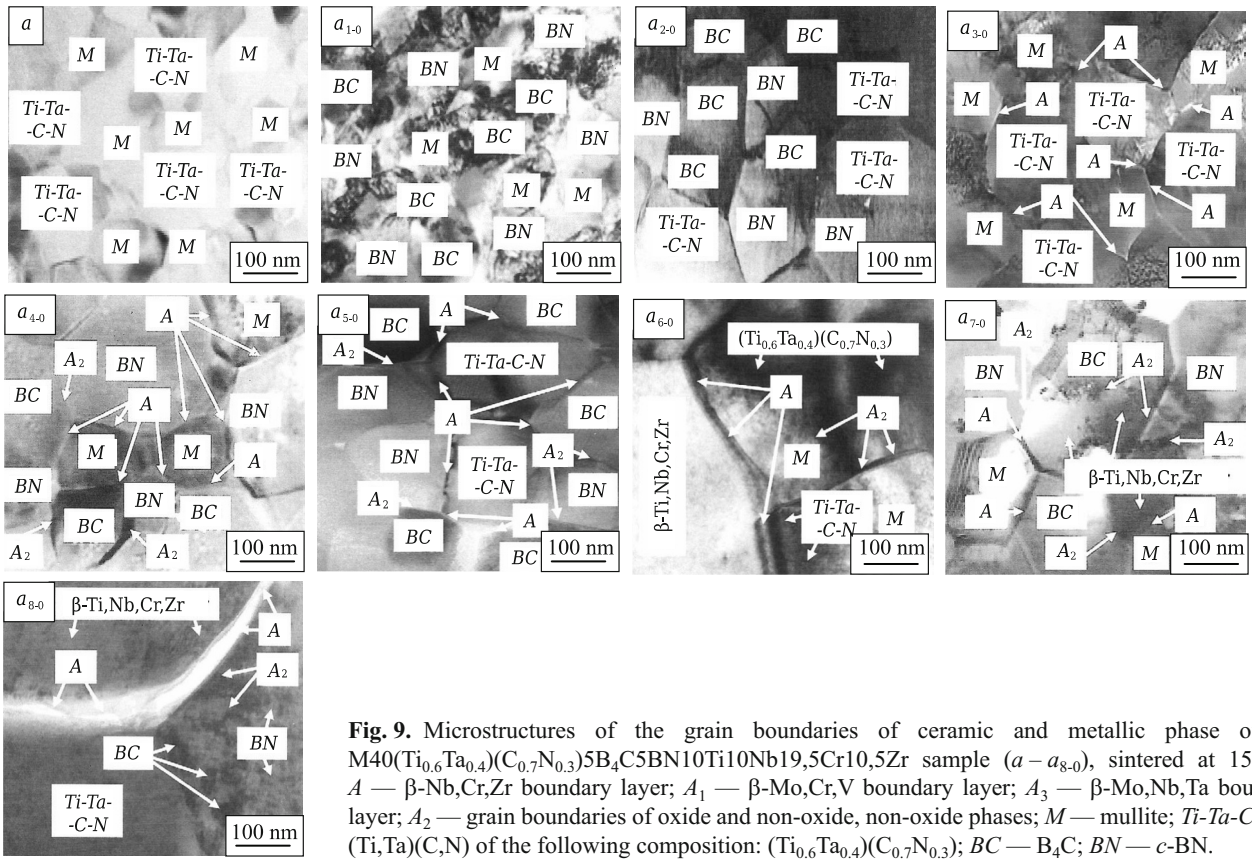

Fig. 9. Microstructures of the grain boundaries of ceramic and metallic phase of the M40($Ti_{0.6}Ta_{0.4}$)($C_{0.7}N_{0.3}$)5B_4C5BN10Ti10Nb19,5Cr10,5Zr sample (a – $a_{8\text{-}0}$), sintered at 1500°C: A — β-Nb,Cr,Zr boundary layer; A_1 — β-Mo,Cr,V boundary layer; A_3 — β-Mo,Nb,Ta boundary layer; A_2 — grain boundaries of oxide and non-oxide, non-oxide phases; M — mullite; *Ti-Ta-C-N* — (Ti,Ta)(C,N) of the following composition: ($Ti_{0.6}Ta_{0.4}$)($C_{0.7}N_{0.3}$); *BC* — B_4C; *BN* — *c*-BN.

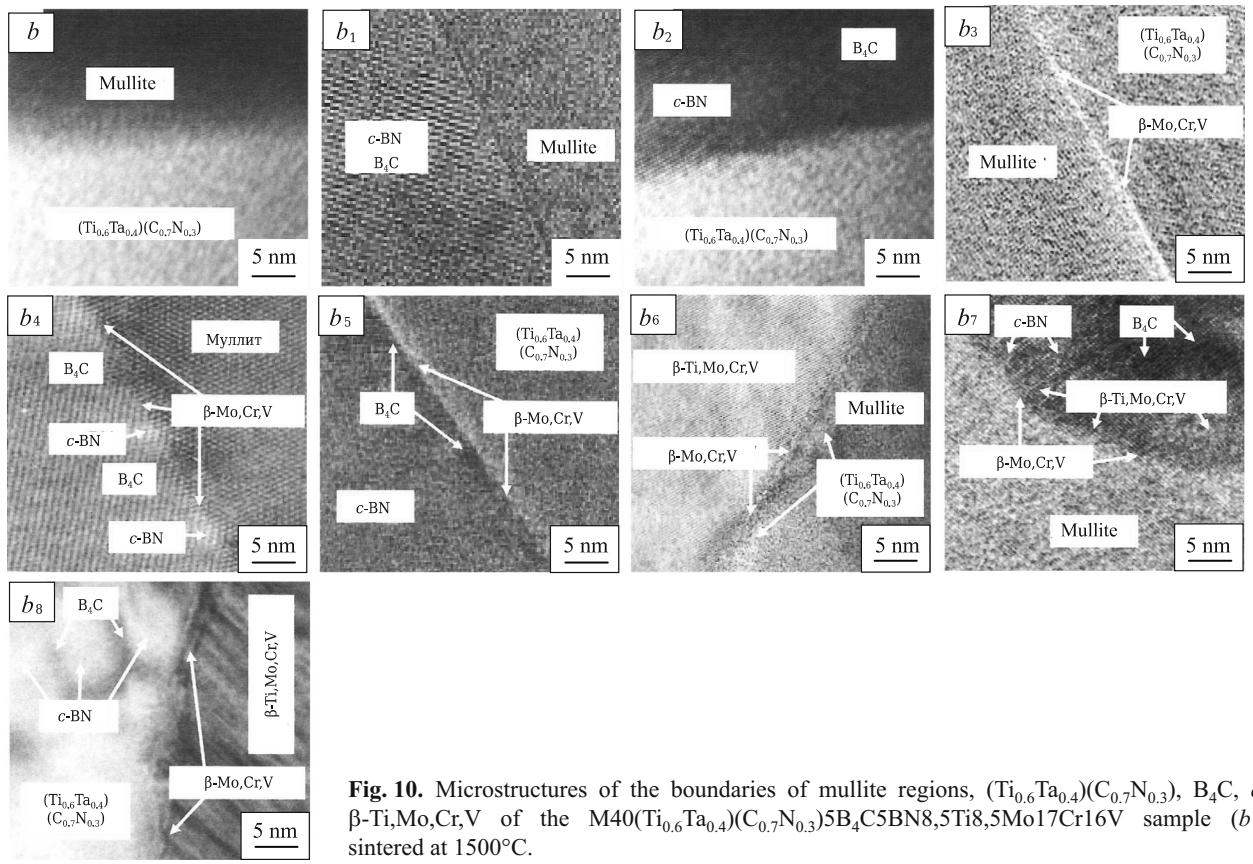

Fig. 10. Microstructures of the boundaries of mullite regions, ($Ti_{0.6}Ta_{0.4}$)($C_{0.7}N_{0.3}$), B_4C, *c*-BN, β-Ti,Mo,Cr,V of the M40($Ti_{0.6}Ta_{0.4}$)($C_{0.7}N_{0.3}$)5B_4C5BN8,5Ti8,5Mo17Cr16V sample (b – b_8), sintered at 1500°C.

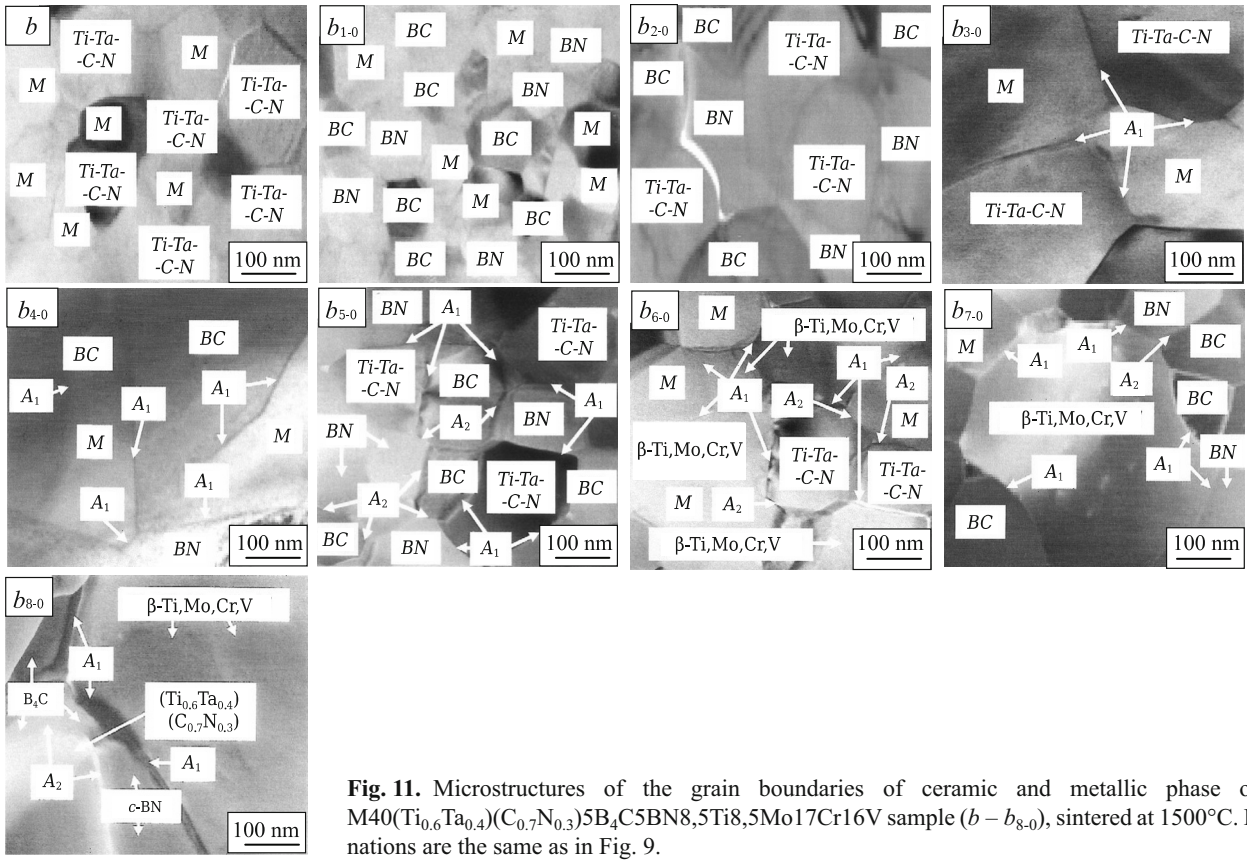

Fig. 11. Microstructures of the grain boundaries of ceramic and metallic phase of the M40($Ti_{0.6}Ta_{0.4}$)($C_{0.7}N_{0.3}$)5B_4C5BN8,5Ti8,5Mo17Cr16V sample (b – $b_{8\text{-}0}$), sintered at 1500°C. Designations are the same as in Fig. 9.

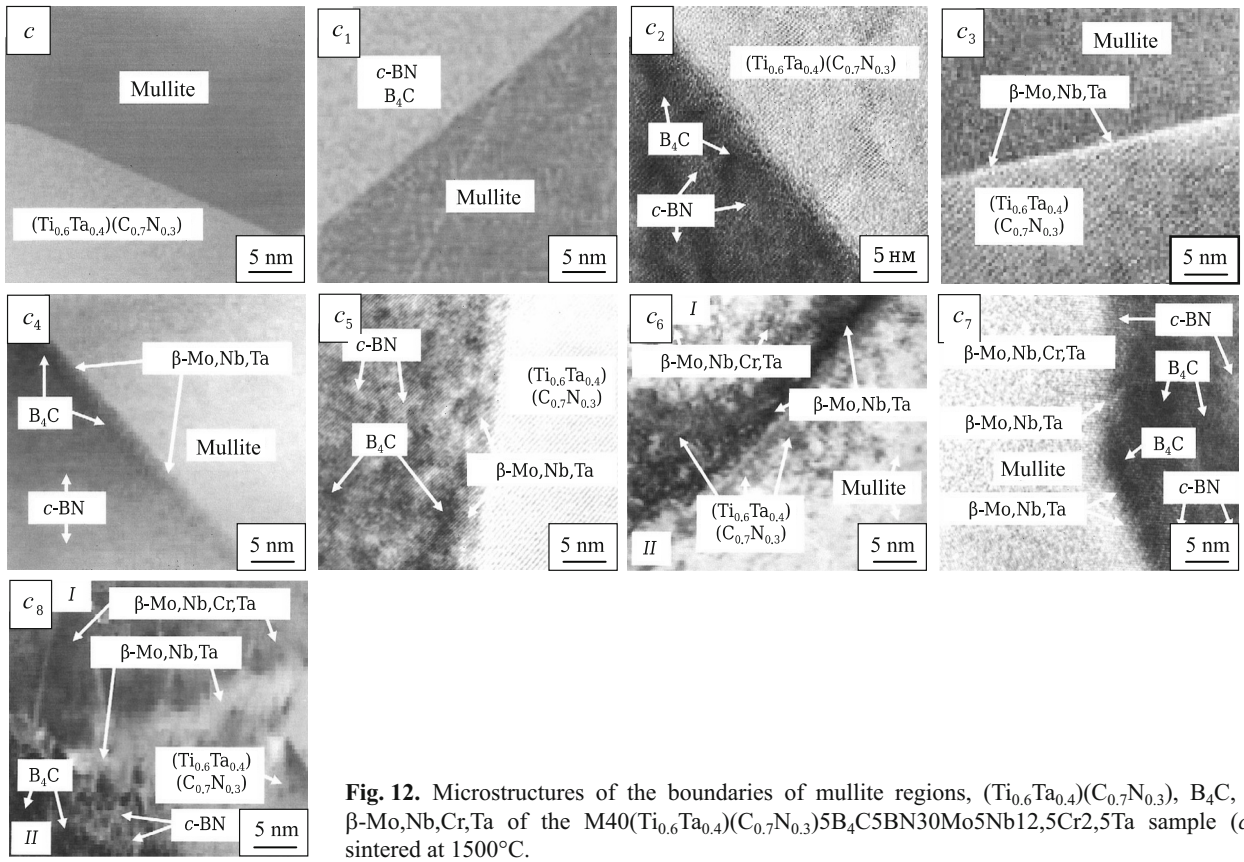

Fig. 12. Microstructures of the boundaries of mullite regions, ($Ti_{0.6}Ta_{0.4}$)($C_{0.7}N_{0.3}$), B_4C, c-BN, β-Mo,Nb,Cr,Ta of the M40($Ti_{0.6}Ta_{0.4}$)($C_{0.7}N_{0.3}$)5B_4C5BN30Mo5Nb12,5Cr2,5Ta sample (c – c_8), sintered at 1500°C.

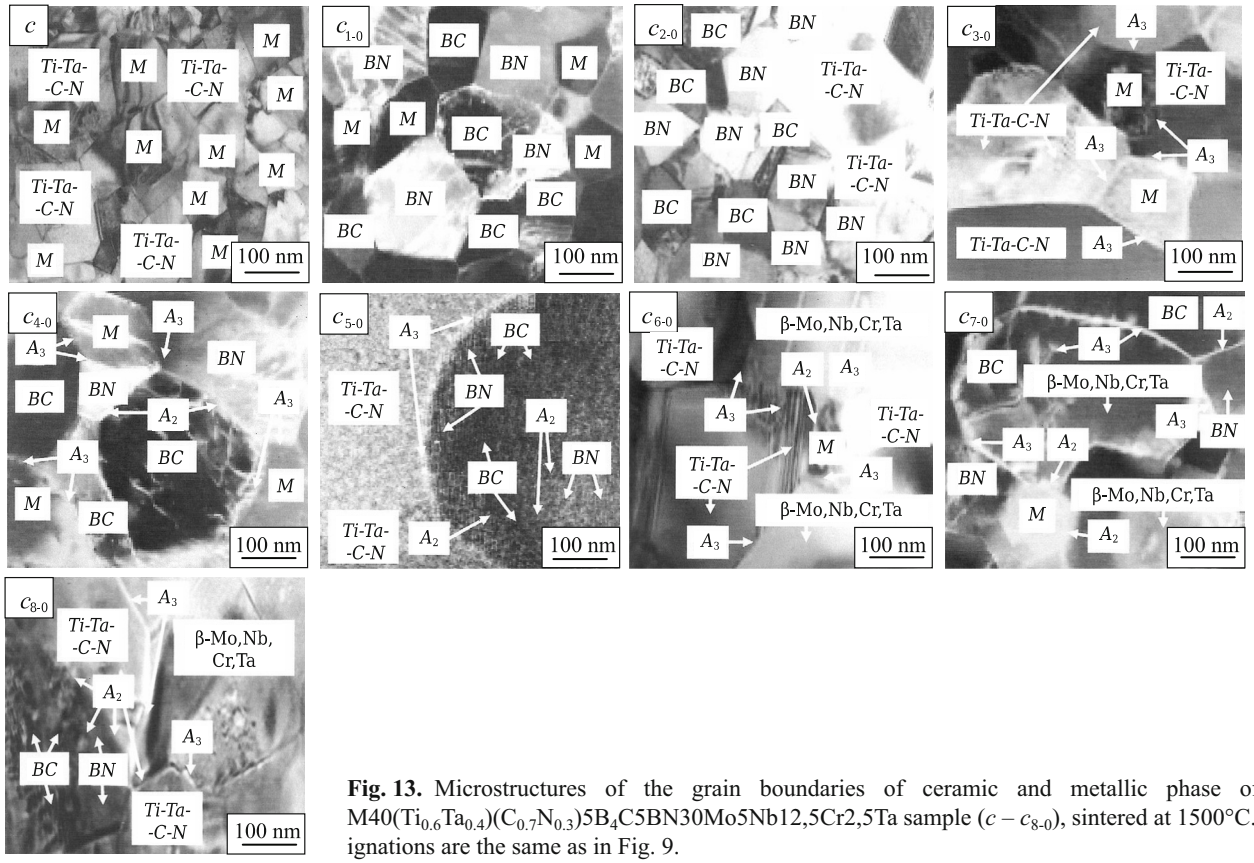

Fig. 13. Microstructures of the grain boundaries of ceramic and metallic phase of the M40($Ti_{0.6}Ta_{0.4}$)($C_{0.7}N_{0.3}$)5B_4C5BN30Mo5Nb12,5Cr2,5Ta sample (c – $c_{8\text{-}0}$), sintered at 1500°C. Designations are the same as in Fig. 9.

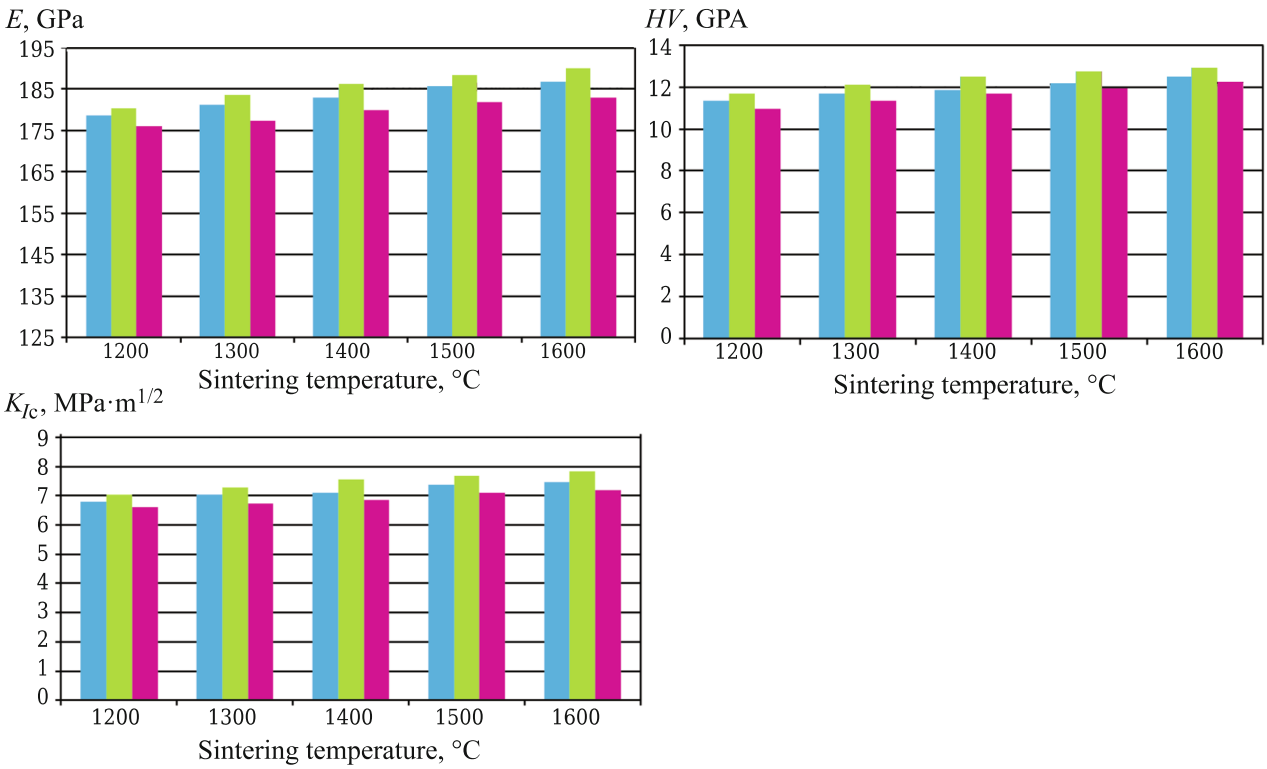

Fig. 14. Variations of E (*a*), K_{Ic} (*b*), and HV (*c*) of the samples: M40($Ti_{0.6}Ta_{0.4}$)($C_{0.7}N_{0.3}$)5B_4C5BN10Ti10Nb19,5Cr10,5Zr (■); M40($Ti_{0.6}Ta_{0.4}$)($C_{0.7}N_{0.3}$)5B_4C5BN8,5Ti8,5Mo17Cr16V (■); (*b*) M40($Ti_{0.6}Ta_{0.4}$)($C_{0.7}N_{0.3}$)5B_4C5BN30Mo5Nb12,5Cr2,5Ta (■); sintered in the range of 1200 – 1600°C.

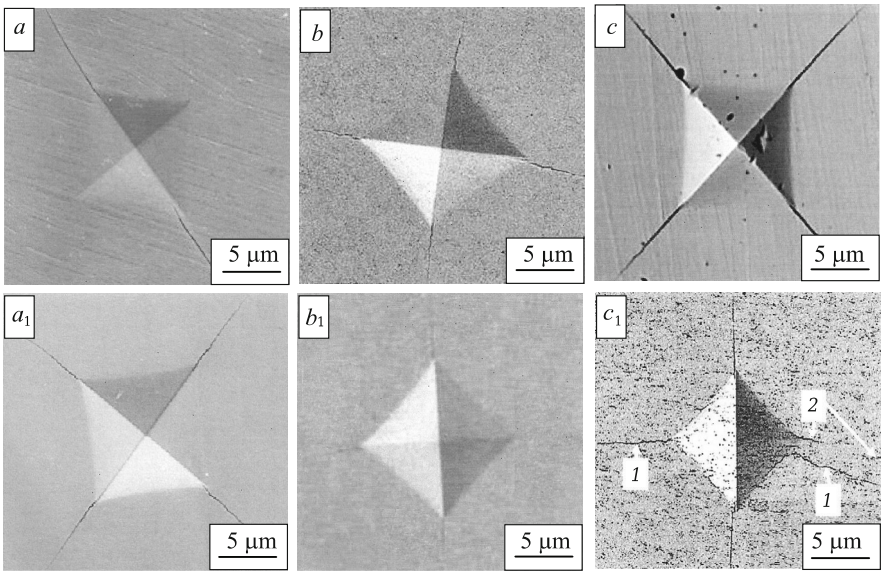

Fig. 15. Path and width of microcracks propagating at the boundaries of particles of ceramic phases and solid solutions of metallic phases of the samples: M40($Ti_{0.6}Ta_{0.4}$)($C_{0.7}N_{0.3}$)5B_4C5BN10Ti10Nb19,5Cr10,5Zr (*a*, a_1); M40($Ti_{0.6}Ta_{0.4}$)($C_{0.7}N_{0.3}$)5B_4C5BN8,5Ti8,5Mo17Cr16V (*b*, b_1); M40($Ti_{0.6}Ta_{0.4}$)($C_{0.7}N_{0.3}$)5B_4C5BN30Mo5Nb12,5Cr2,5Ta (*c*, c_1), sintered at 1300°C (*a*, *b*, *c*) and 1500°C (a_1, b_1, c_1): *1*) main microcrack; *2*) secondary microcrack.

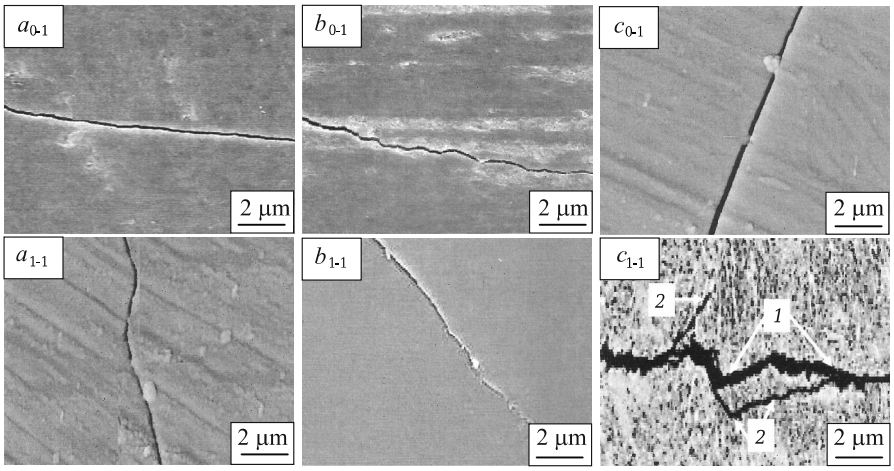

Fig. 16. Indentation images when measuring *HV* of the samples: *a*, a_1) M40($Ti_{0.6}Ta_{0.4}$)($C_{0.7}N_{0.3}$)5B_4C5BN10Ti10Nb19,5Cr10,5Zr; *b*, b_1) M40($Ti_{0.6}Ta_{0.4}$)($C_{0.7}N_{0.3}$)5B_4C5BN8,5Ti8,5Mo17Cr16V; *c*, c_1) M40($Ti_{0.6}Ta_{0.4}$)($C_{0.7}N_{0.3}$)5B_4C5BN30Mo5Nb12,5Cr2,5Ta, sintered at 1300°C (*a*, *b*, *c*) and 1500°C (a_1, b_1, c_1): *1*) main microcrack; *2*) secondary microcrack.

shown by the sample, containing a mixture of Ti, Mo, Cr, and V powders, compared to a less active increase of such properties observed in samples, containing mixtures of Ti, Nb, Cr, Zr and Mo, Nb, Cr, Ta powders, in the temperature range of 1200 – 1600°C.

The lower values of the physico-mechanical properties of the sample with a mixture of Ti, Nb, Cr, and Zr powders up to 1400°C are caused by a non-homogeneous and gradual solid-phase crystallization of a less dense structure of the α-Ti,Nb,Cr,Zr phase (see Fig. 4*a*), less uniform and weakly sintered microstructure with a large number of different sizes of pores (see Fig. 5*a*), and a development of monodisperse composition of grains of the crystalline phases (see Fig. 6). This leads to a considerable decrease in strengthening, rigidity, hardness, and reinforcing of the boundary areas of the particles of B_4C and α-Ti,Nb,Cr,Zr; *c*-BN and α-Ti,Nb,Cr,Zr; (Ti,Ta)(C,N) and α-Ti,Nb,Cr,Zr; as well as B_4C, *c*-BN, and (Ti,Ta)(C,N) with high heterogeneity of local stress sites around brittle α-Ti,Nb,Cr,Zr particles and low distribution of ductile properties at the boundary areas of these heterogeneous particles. As a result, there is a reduction in crack resistance, where are visible a rectilinear path, slightly wide and longer microcracks in the photo of indenta-

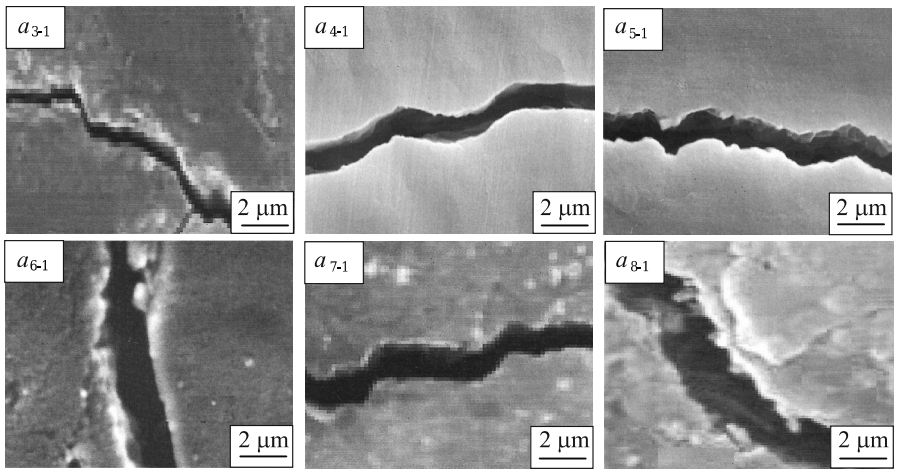

Fig. 17. Microcrack propagation across the boundary layer of solid solution of metallic phase of the M40($Ti_{0.6}Ta_{0.4}$)($C_{0.7}N_{0.3}$) 5B_4C5BN10Ti10Nb19,5Cr10,5Zr sample ($a_{3\text{-}1} - a_{8\text{-}1}$), sintered at 1500°C.

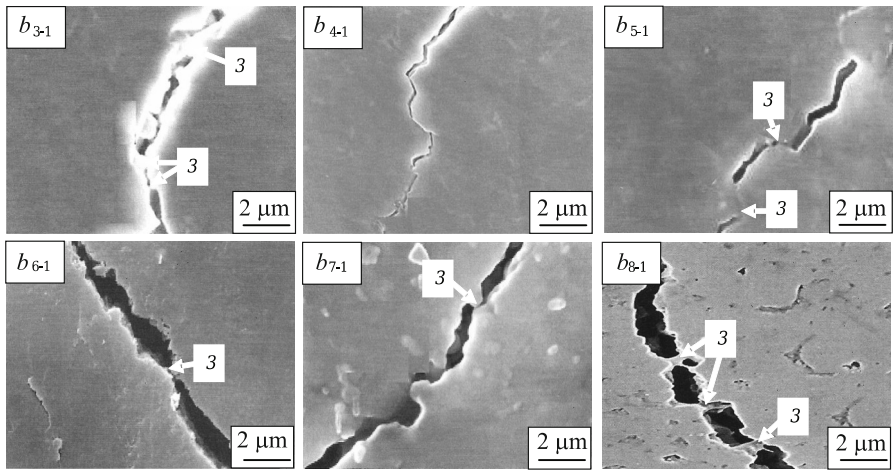

Fig. 18. Microcrack propagation across the boundary layer of solid solution of metallic phase of the M40($Ti_{0.6}Ta_{0.4}$)($C_{0.7}N_{0.3}$) 5B_4C5BN8,5Ti8,5Mo17Cr16V sample ($b_{3\text{-}1} - b_{8\text{-}1}$), sintered at 1500°C: *3*) bridges across microcracks.

tion press (see Fig. 14*a*), at the interface of ceramic particles and solid solution of metallic phase (see Fig. 16$a_{0\text{-}1}$), caused by the localization of brittleness areas around the α-Ti,Nb,Cr,Zr particles and large sizes of pores at the boundary areas of the grains (see Fig. 5*a*). In a result, the initiation of such microcracks requires minimum energy and, occurs easily and more quickly. This leads to a non-homogeneous dissipation of the stress sites in front of the propagating microcracks. A higher increase of the values of such properties of the sample with a mixture of Ti, Nb, Cr, and Zr powders in the temperature range of 1400 – 1600°C is associated with the activation of liquid-phase crystallization of a more dense structure of β-Ti,Nb,Cr,Zr (see Fig. 4*a*), development of a uniform and densely sintered microstructure with the absence of pores (see Fig. 5a_1), more variously-dispersed composition of grains of the crystalline phases (see Fig. 6), formation of various dense, relatively uniform, slightly torturous, and various-width boundary layers of the β-Nb,Cr,Zr phase (see Fig. 8$a - a_8$), and relatively dense packing with clear boundary areas of oxide and non-oxide particles, non-oxide particles and particles of solid solution of the metallic phase (see Fig. 9$a - a_{8\text{-}0}$), with different paths and various-width of microcracks across the boundary layers of solid solution of the metallic phase (see Fig. 17$a_{3\text{-}1} - a_{8\text{-}1}$). This leads to a certain increase of strengthening, rigidity, hardness, and reinforcing of the boundary areas of the particles B_4C and β-Ti,Nb,Cr,Zr; *c*-BN and β-Ti,Nb,Cr,Zr; (Ti,Ta)(C,N) and β-Ti,Nb,Cr,Zr; and B_4C, *c*-BN, and (Ti,Ta)(C,N) with a reduction of local stresses and a higher distribution of ductile properties at the boundaries of such heterogeneous particles. This improves crack resistance with the formation of some tortuosity, less wide and longer microcracks in the photo of indentation press (see Fig. 15a_1), at the boundary of the ceramic particles and particles of solid

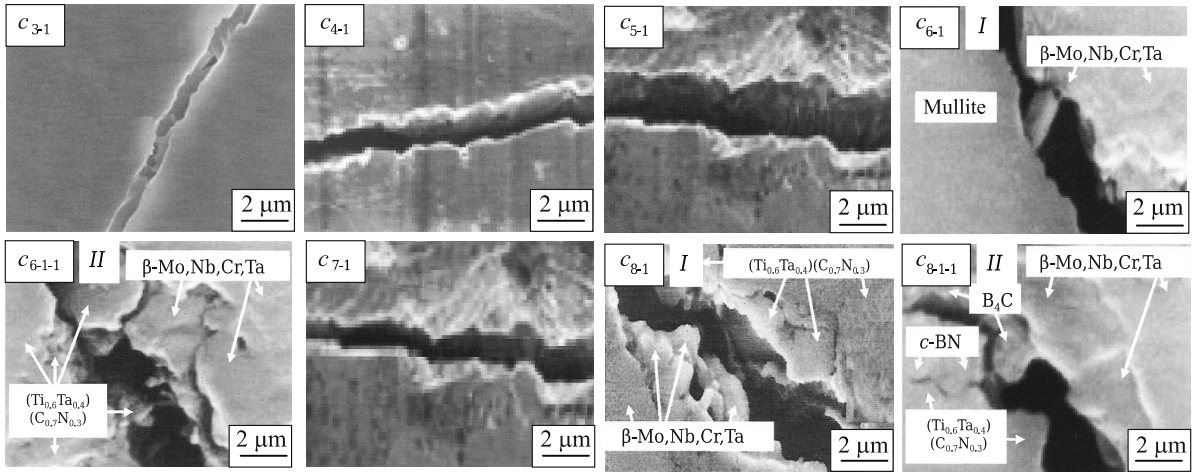

Fig. 19. Microcrack propagation across the boundary layers of solid solution of metallic phase of the M40($Ti_{0.6}Ta_{0.4}$)($C_{0.7}N_{0.3}$) 5B_4C5BN30Mo5Nb12,5Cr2,5Ta sample ($c_{3\text{-}1} - c_{8\text{-}1\text{-}1}$), sintered at 1500°C: *I, II* — microcracks propagation across the upper and lower areas of boundary layers of the solid solution of metallic phase.

solution of the metallic phase (see Fig. 16$a_{1\text{-}1}$) associated with higher energy for initiation of microcracks with the partial dissipation of stress sites in front of the propagating microcracks.

A higher increase of the physico-mechanical properties of the sample with a mixture of Ti, Mo, Cr, and V powders up to 1400°C is caused by active solid-phase crystallization of a more dense structure of the α-Ti,Mo,Cr,V phase (see Fig. 4*b*), more uniform and densely sintered microstructure with a small number of pores (see Fig. 5*b*), development of more variously-dispersed compositions of grains of the crystalline phases (see Fig. 6). In a result increase strengthening, rigidity, hardness, and reinforcing of the boundary regions of the particles of B_4C and α-Ti,Mo,Cr,V; *c*-BN and α-Ti,Mo,Cr,V; (Ti,Ta)(C,N) and α-Ti,Mo,Cr,V; as well as non-oxide particles with a significant reduction of the number of local stress sites and uniform distribution of ductile properties at the boundaries of such heterogeneous particles. This improves crack resistance with the evolution of torturous path, narrow, small length of microcracks in the photo of indentation press (see in Fig. 15*b*), at the boundary of ceramic particles and solid solution of metallic phases (see Fig. 16$b_{0\text{-}1}$). As a result, the stress sites are dissipated more actively in front of propagating microcracks. The most active increase and higher values of such properties of the sample in the temperature range of 1400 – 1600°C are associated with intensive liquid-phase crystallization of the dense structure of the β-Ti,Mo,Cr,V phase (see Fig. 4*b*), development of a uniform and densely sintered microstructure with a small number of pores (see Fig. 5b_1), a more diverse composition of grains of the crystalline phase (see Fig. 6), formation of dense, homogeneous, torturous, and narrow boundary layers of the β-Mo,Cr,V phase (see Fig. 10$b - b_8$), dense packing with barely visible boundary areas of oxide and non-oxide particles, non-oxide particles and particles of solid solution of the metallic phase (see Fig. 11$b - b_{8\text{-}0}$)), with tapering, torturous, intermittent path of narrow microcracks across the boundary layers of solid solution of the metallic phase, in the middle of them are located variety of dense, small strengthening and reinforcing bridges (see Fig. 17$a_{3\text{-}1} - a_{8\text{-}1}$). As a result, significantly increase in strengthening, rigidity, hardness, and rein-forcing the boundary areas of the particles of B_4C and β-Ti,Mo,Cr,V; *c*-BN and β-Ti,Mo,Cr,V; (Ti,Ta)(C,N) and β-Ti,Mo,Cr,V; as well as B_4C, *c*-BN, and (Ti,Ta)(C,N) with the largest dissipation of local stresses and uniform distribution of ductile properties at the boundaries of such particles. Therefore, significantly improves the crack resistance with the formation of torturous path, narrow and short microcracks in the photo of indentation press (see the Fig. 15b_1), at the boundary of ceramic particles and solid solution of the metallic phase (see Fig. 16$b_{1\text{-}1}$). Due to dense, hard particles of B_4C, *c*-BN, (Ti,Ta)(C,N), β-Ti,Mo,Cr,V and the presence of small pores (see Fig. 5b_1), the initiation of such microcracks requires maximum energy and is strongly hindered. As a result, stress sites are actively dissipated in front of the propagating microcracks.

The lowest values of the physico-mechanical properties of the sample with a mixture of Mo, Nb, Cr, and Ta powders, in the temperature range of 1200 – 1600°C are caused by non-homogeneous and gradual solid-phase crystallization of a less dense structure of the α-, β-Mo,Nb,Cr,Ta phases (see Fig. 4*c*), non-uniform and non - densely sintered microstructures with a large number of different sizes of pores (see Fig. 5*c*, c_1), development of more monodisperse compositions of grains of the crystalline phases (see Fig. 6), formation of non-homogeneous, variously dense, rectilinear, and wide boundary layers of the β-Mo,Nb,Ta phase (see Fig. 12$c - c_8$), non-homogeneously dense and partially layered compaction with strongly visible boundary sections of oxide and non-oxide particles, non-oxide par-ticles and parti-

cles of solid solution of the metallic phase (see Fig. 13*c* – $c_{8\text{-}0}$), different path, width, and homogeneity of microcracks across the boundary layers of solid solution of the metallic phase (see Fig. 19$c_{3\text{-}1}$ – $c_{8\text{-}1}$) during active cracking of the brittle boundary structures of the intermediate layers of β-Mo,Nb,Ta, especially near the β-Mo,Nb,Cr,Ta particles with the crumbling of area of such particles and the formation of different size of β-Mo,Nb,Cr,Ta particles (see Fig. 19$c_{8\text{-}1}$, comparing to various resistance to crumbling the areas with the B_4C, *c*-BN particles, higher with the (Ti,Ta)(C,N) particles, which differently retards the propagation and reduces the width of microcracks across the boundary layer of β-Mo,Nb,Ta (see Fig. 19$c_{6\text{-}1}$, $c_{6\text{-}1\text{-}1}$, $c_{8\text{-}1}$, $c_{8\text{-}1\text{-}1}$). This indicates the different homogeneity, completeness of solid-phase diffusion processes, and sintering of the intermediate layer of β-Mo,Nb,Ta and the particles of B_4C, *c*-BN, (Ti,Ta)(C,N), β-Mo,Nb,Cr,Ta. During these processes, there is no crumbling of the particles, which is associated with high density and hardness of such particles. As a result, reduce strengthening, rigidity, hardness, and reinforcing of the boundary areas of the particles B_4C and α-, β-Mo,Nb,Cr,Ta; *c*-BN and α-, β-Mo,Nb,Cr,Ta; (Ti,Ta)(C,N) and α-, β-Mo,Nb,Cr,Ta; as well as B_4C, *c*-BN, and (Ti,Ta)(C,N) with a non-homogeneous increase of local stress sites around the less hard α-, β-Mo,Nb,Cr,Ta particles, and a low distribution of ductile properties in the boundary areas of such heterogeneous particles. As a result, more reduces the crack resistance, where visible clear rectilinear path, more wide and more long the main microcracks with small tortuosity at the ends, with various sizes of certain chips (see Fig. 15*c*), towards brittle areas are formed, as well as the combination of different paths and widths of the main and secondary microcracks in the photo of indentation press (see Fig. 15c_1), at the boundary of the ceramics particles and solid solution of the metallic phases (see. Fig. 16$c_{0\text{-}1}$, $c_{1\text{-}1}$). This is caused by the formation of large brittle areas around the α-, β-Mo,Nb,Cr,Ta particles and large sizes of pores at the boundary sections of the grains (see Fig. 5*c*, c_1). As a result, the initiation of such microcracks requires minimum energy and, occurs easily and more quickly. Thus, in front of propagating the main microcrack of a larger width and with the rectilinear path are localized and more non-uniformly dissipated significant stress sites along the β-Mo,Nb,Cr,Ta particles and between the (Ti,Ta)(C,N) and β-Mo,Nb,Cr,Ta particles. Such microcrack undergoes a significant narrowing between the B_4C and *c*-BN particles, and the stress sites in front of it are dissipated more actively. The stress sites are also intensively dissipated in front of a torturous, secondary, narrow microcrack between the *c*-BN and (Ti,Ta)(C,N) particles with partial retarding of propagation the microcrack (see Fig. 19$c_{1\text{-}1}$, $c_{8\text{-}1\text{-}1}$). Thus, the strengthening and reinforcing of boundary regions of the *c*-BN and (Ti,Ta)(C,N) particles is higher, than the boundary regions of the B_4C and *c*-BN particles, and (Ti,Ta)(C,N) and β-Mo,Nb,Cr,Ta particles.

The results of the physico-mechanical properties differently affect S_x and ΣS_x, as well as linear correlation of E and K_{Ic} of the samples in the temperature range of 1200 – 1600°C (Fig. 20).

The arrangement of values (points) relative to the standard deviation ranges for E and K_{Ic} of the samples with mixtures of Ti, Nb, Cr, Zr and Ti, Mo, Cr, V powders, is generally similar with a more uneven arrangement of values relative to the standard deviation ranges for E and K_{Ic} of the sample with a mixture of Ti, Mo, Cr, V powders. A more uniform arrangement of values (points) relative to the standard deviation ranges for E and K_{Ic} of the sample with a mixture of Mo, Nb, Cr, and Ta powders. These differences affect the value of mean S_x at each temperature, the total value of ΣS_x of linear correlation E and K_{Ic} of the samples in the temperature range of 1200 – 1600°C, where more low total values of standard deviations with a mixture of Ti, Mo, Cr, and V powders, higher total values — in the sample with a mixture of Ti, Nb, Cr, and Zr powders, and the highest total values - in the sample with a mixture of Mo, Nb, Cr, and Ta powders in the temperature range of 1200 – 1600°C. This is related with a different variation of data scattering relative to each other and a certain value relative to mean value of E and K_{Ic} at each temperature, that affects the accuracy of mean value of S_x of E and K_{Ic} at a current temperature, in result at the value and accuracy of total value of standard deviations of E and K_{Ic} in the range of 1200 – 1600°C. In this case, the scattering of E and K_{Ic} values is reduced significantly in the samples with mixtures of Ti, Nb, Cr, Zr and Ti, Mo, Cr, V powders, as opposed to a gradual decrease in such scattering of the property values of the sample with a mixture of Mo, Nb, Cr, and Ta powders, as the temperature increases from 1200 to 1600°C.

Comparing the R^2 values, are visible small differences of R^2 of the samples with mixtures of Ti, Nb, Cr, Zr and Mo, Nb, Cr, Ta; Ti, Mo, Cr, V and Mo, Nb, Cr, Ta powders, equal to 0,01 and 0,02, compared to the R^2 difference of the samples with mixtures of Ti, Nb, Cr, Zr and Ti, Mo, Cr, V powders, equal to 0,0108. These R^2 differences correlate with the arrangement of E and K_{Ic} values of the samples relative to straight lines, as well as with the total values of standard deviations of E and K_{Ic} in the temperature range of 1200 – 1600°C. The correlation accuracy of the property values of the sample with a mixture of Ti, Nb, Cr, and Zr powders increases in the range of 1400 – 1600°C compared to practically unchanged and high correlation accuracy of the sample with a mixture of Ti, Mo, Cr, and V powders in the range of 1200 – 1600°C and non-uniform (low) correlation accuracy of the sample with a mixture of Mo, Nb, Cr, and Ta powders, relative to straight lines in the temperature range of 1200 – 1600°C. In this case, the E and K_{Ic} values of the sample with a mixture of Ti, Mo, Cr, and V powders, are located on a straight line, slightly shifted, and more shifted relative to the straight lines of the samples with mixtures of Ti, Nb, Cr, Zr and Mo, Nb, Cr, Ta powders in the range of

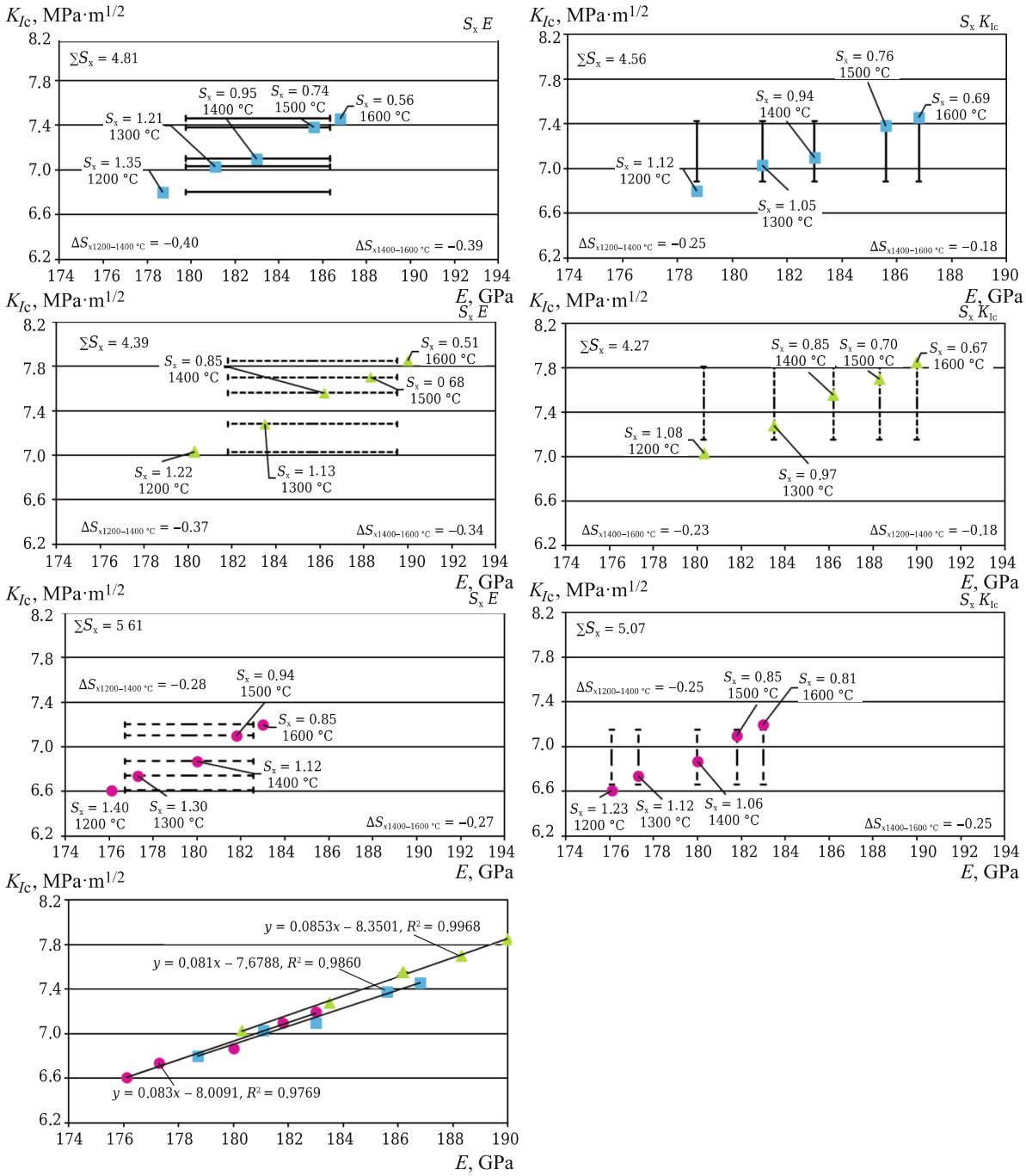

Fig. 20. Values of S_x and ΣS_x, as well as linear correlation of E and K_{Ic} of the samples: M40($Ti_{0.6}Ta_{0.4}$)($C_{0.7}N_{0.3}$)5B_4C5BN10Ti 10Nb19,5Cr10,5Zr (■); M40($Ti_{0.6}Ta_{0.4}$)($C_{0.7}N_{0.3}$)5B_4C5BN8,5Ti8,5Mo17Cr16V (▲); M40($Ti_{0.6}Ta_{0.4}$)($C_{0.7}N_{0.3}$)5B_4C5BN30Mo5Nb12,5Cr2,5Ta (●) in the range of 1200 – 1600°C.

1200 – 1600°C, respectively. Also, the arrangement of the straight lines does not differ relative to each other.

The differences of mismatches of standard deviations values in each of the temperature ranges, the total standard deviations values, and correlation of the E and K_{Ic} values relative to the straight lines with the difference in the R^2 value of the samples in the range of 1200 – 1600°C are associated with the differences of the reaction mechanisms, intensity of solid-/liquid-phase crystallization, and density of structures of the α-, β-Ti,Nb,Cr,Zr; α-, β-Ti,Mo,Cr,V; and α-, β-Mo,Nb,Cr,Ta phases (see reactions (7) – (23) and Fig. 4a – c), as well as homogeneity and density of the sintered microstructures (see Fig. 5a – c, a_1 – c_1), dispersity of the crystal phase grain composition (see Fig. 6), uniformity, density of structures, path, width of the boundary layers of solid solutions of metallic phases (see Fig. 8a – a_8,

$10b - b_8$, $12c - c_8$), packing of non-oxide particles and particles of solid solutions of metallic phases (see Fig. $9a - a_{8\text{-}0}$, $11b - b_{8\text{-}0}$, $13c - c_{8\text{-}0}$), as well as microcracks propagating path, width, length across the boundary layers of different solid solutions of metallic phases (see Fig. $17a_{3\text{-}1} - a_{8\text{-}1}$, $18b_{3\text{-}1} - b_{8\text{-}1}$, $19c_{3\text{-}1} - c_{8\text{-}1\text{-}1}$). As a result, the strengthening and reinforcing effect of the various-dense structures of the α-, β-Ti,Nb,Cr,Zr and α-, β-Ti,Mo,Cr,V phases, cermet microstructures, as well as (Ti,Ta)(C,N), B_4C, *c*-BN and β-Ti,Nb,Cr,Zr and β-Ti,Mo,Cr,V particles on the uniformity, path, width of structures of the boundary layers of solid solutions of metallic phases, microcracks at the boundaries of ceramic particles and solid solutions of metallic phases, across the boundary layers of solid solutions of metallic phases, as well as the effect of the boundary layers of solid solutions of metallic phases on the strengthening and reinforcing the structures of the samples with mixtures of Ti, Nb, Cr, Zr and Ti, Mo, Cr, V powders, is approximately similar. This correlates with small differences of ΣS_x and R^2 for E and K_{Ic} (equal to 0,42, 0,29, and 0,0108, respectively) unlike a different strengthening and reinforcing effect of the various dense structures of α-, β-Ti,Nb,Cr,Zr; α-, β-Ti,Mo,Cr,V; and α-, β-Mo,Nb,Cr,Ta, cermet microstructures, (Ti,Ta)(C,N), B_4C, *c*-BN particles and solid solutions of metallic phases, boundary layers of solid solutions of metallic phases of the samples with mixtures of Ti, Nb, Cr, Zr and Mo, Nb, Cr, Ta, and Ti, Mo, Cr, V and Mo, Nb, Cr, Ta powders. In this case, such differences are more pronounced between the samples with mixtures of Ti, Mo, Cr, V and Mo, Nb, Cr, Ta powders, rather than between the samples with mixtures of Ti, Nb, Cr, Zr and Mo, Nb, Cr, Ta powders. This indicates various differences of values of ΣS_x and R^2 for E and K_{Ic} (1,22, 0,80, and 0,02 versus 0,80, 0,51, and 0,01, respectively).

CONCLUSION

The effect of the mixtures of Ti, Nb, Cr, Zr; Ti, Mo, Cr, V; and Mo, Nb, Cr, Ta powders on the phase composition, microstructure, grain sizes of crystalline phases, ρ_{rel}, Δl, physico-mechanical properties, linear correlation, values of standard deviations for E and K_{Ic} of mullite – (Ti,Ta)(C,N) – B_4C – *c*-BN samples is shown during spark plasma sintering of compositions at a pressing load of 85 MPa in the temperature range of 1200 – 1600°C.

The synthesized TiC, TiN, B_4C, and *h*-BN powders are characterized by respectively different crystallization intensity of the TiC, TiN, B_4C, and *h*-BN phases. A (Ti,Ta)(C,N) solid solution, obtained by spark plasma sintering at 1500°C, shows an intensive crystallization of the (Ti,Ta)(C,N) phase along with the crystalline, uniform, densely sintered microstructure, and consists of uniformly packed grains of (Ti,Ta)(C,N).

The sintered samples with mixtures of metal powders, show intensive mullitization, active crystallization of (Ti,Ta)(C,N) and less intensive crystalline phases of B_4C and *c*-BN with various evolution of crystalline phases of β-Ti,Nb,Cr,Zr; β-Ti,Mo,Cr,V; and β-Mo,Nb,Cr,Ta in the temperature range of 1200 – 1600°C. The sample with a mixture of Ti, Nb, Cr, and Zr powders, forms a more uniform and densely sintered microstructure at 1500°C, as well as variously-dispersed grain compositions of crystalline phases in the range of 1200 – 1600°C. This composition undergoes more intensive sintering, however, forms less homogeneous and non-dense structure, more wide and less tortuous boundary layers of solid solution of the metallic phase, across them propagating microcracks with different path and width unlike the sintered composition with a mixture of Ti, Mo, Cr, V powders and with higher properties of boundary layers, microcracks comparing to the composition with a mixture of Mo, Nb, Cr, Ta powders at 1500 °C. As a result, the sample with a mixture of Ti, Mo, Cr, and V powders shows a higher increase of the physico-mechanical property values, higher crack resistance, higher linear correlation, and smaller values of mean and total standard deviations of the modulus of elasticity and fracture toughness in the temperature range of 1200 – 1600°C.

REFERENCES

1. D. Jianxin and S. Junlong, "Microstructure and mechanical properties of hot-pressed B_4C/TiC/Mo ceramic composites," *Ceram. Int.*, **35**(2), 771 – 778 (2009).
2. G. Ehsan and M. Shahedi, "Microstructural development during spark plasma sintering of ZrB_2-SiC-Ti composite," *Ceram. Int.*, **44**, 15 (2018).
3. R. Vedant, H. Parshad, and P. Jain, "Development of ZrB_2–B_4C–Mo ceramic matrix composite for high temperature applications," *Global J. Eng. Sci. Resear.*, **6**(6), 490 – 505 (2019).
4. N. Behzad, A. Zohre, S. A. Mehdi, and P. Soroush, "Influence of vanadium content on the characteristics of spark plasma sintered ZrB_2–SiC–V composites," *J. All. Comp.*, **805**, 725 – 732 (2019).
5. A. V. Hmelov, "Development of oxide-free oxide materials under spark-plasma sintering conditions of a mixture of oxide-free components and various metal powder additives," *Refract. Ind. Ceram.*, **61**(1), 73 – 81 (2020).
6. A. V. Hmelov, Development of dense materials by spark plasma sintering of oxide-nonoxide components with different mixtures of metal powders," *Refract. Ind. Ceram.*, **61**(3), 313 – 321 (2020).
7. A. V. Hmelov, "Spark plasma sintering of oxide-nonoxide components with the addition of a TiC–ZrC solid solution and various metal powder mixtures," *Refract. Ind. Ceram.*, **61**(5), 568 – 579 (2021).
8. A. V. Hmelov, "Stimulation of spark-plasma sintering of mixtures of oxide-non-oxide components by adding a solid solution TaB_2–NbC and through a nickel melt in mixtures of metal powders," *Refract. Ind. Ceram.*, **62**(1), 74 – 88 (2021).
9. A. V. Hmelov, "Development of dense and hard materials based on oxide-non-oxide compounds with added intermetallic components during spark plasma sintering," *Refract. Ind. Ceram.*, **62**(5), 570 – 586 (2022).

10. S. F. Jawed, C. D. Robadia, Y. J. Liu, and L. Q. Wang, "Beta-type Ti–Nb–Cr–Zr alloys with large plasticity and significant strain hardening," *Materials and Design*, **181**(5), 134 – 140 (2019).
11. B. Hu, J. Wang, C. Wang, Y. Du, and J. Zhu, "Thermodynamic assessment of the Ti–Mo–Cr–V quaternary system," *Comp. Coumpling Phase Diag. Thermochem*., **55**(2), 103 – 112 (2016).
12. L. Peng, S. Takizawa, T. Horiuchi, and S. Miura, "Effect of Si on the stability of $NbCr_2$ phase in Cr–Nb–Mo system," *Intermetallics*., **110**(5), 1 – 7 (2019).
13. E. J. Cheng, H. Katsui, and T. Goto, "Rod-like eutectic structure of arc-melted TiB_2–TiC_xN_{1-x} composite," *J. Eur. Ceram. Soc.*, **34**(9), 2089 – 2094 (2014).
14. A. V. Hmelov, "Preparation of mullite–TiC–TiN materials by a spark plasma method with high compaction loading and their properties," *Refract. Ind. Ceram.*, **59**(3), 262 – 268 (2018).
15. M. Szutkowska, L.-L. Jolanta, and C. Jolanta, "Properties of TiC and TiN reinforced alumina-zirconia composites sintered with spark plasma technique," *Metals*, **9**(11), 1220 – 1234 (2019).
16. M. Naidoo, J. Oluwagbenga, I. Sigalas, and M. Herrmann, "Preparation of (Ti,Ta)(C,N) by mechanical alloying Ti(C,N) and TaC," *Int. J. Refract. Met. Hard Mater.,* **37**(2), 67 – 72 (2013).
17. M. Naidoo, J. Raethel, I. Sigalas, and M. Herrmann, "Preparation of (Ti,Ta)(C,N) by mechanical alloying," *Int. J. Refract. Met. Hard Mater.*, **35**(1), 178 – 185 (2012).
18. H. Zhang, M. Fu, L. Ma, S. Gu, and J. Liu, "Fabrication and properties of (Ti,W,Mo,Nb,Ta)(C,N)–Co–Ni cermets," *J. Mat. Eng. Perfor.*, **28**(12), 7198 – 7205 (2019).